
Article:

Shi, Y., Li, S., Chen, H. et al. (2 more authors) (2018) Improved SPH simulation of spilled oil contained by flexible floating boom under wave-current coupling condition. Journal of Fluids and Structures, 76. pp. 272-300. ISSN 0889-9746

https://doi.org/10.1016/j.jfluidstructs.2017.09.014

Improved SPH simulation of spilled oil contained by flexible floating boom under wave-current coupling condition

Yang Shi [a], Shaowu Li [a*], Hanbao Chen [b], Ming He [a], Songdong Shao[c]

[a] State Key Laboratory of Hydraulic Engineering Simulation and Safety, Tianjin University, Tianjin 300072, China

[b] Tianjin Research Institute for Water Transport Engineering, Ministry of Transport of China, Tianjin 300456, China

[c] Department of Civil and Structural Engineering, University of Sheffield, Sheffield S1 3JD, United Kingdom

[*] Corresponding author, E-mail: lishaowu@tju.edu.cn

ABSTRACT

A multi-phase Smoothed Particle Hydrodynamics (SPH) method is developed to model the failure process of a flexible oil boom. An algorithm is proposed based on the dynamic boundary particles (DBPs) for preventing the particle disorders during the multi-fluid particle movement around the solid boundary. The improved multi-phase SPH model is firstly validated by the experimental data of a wedge falling into a two-layer oil-water fluid. Then a numerical wave-current flume is established with an active absorbing piston-type wave generator and a circulating current system. The model reliability is validated against the measured vertical profiles of velocity. Simulation of the flexible floating boom movement is implemented by introducing a Rigid Module and Flexible Connector (RMFC) multi-body system. The model is finally applied to the simulation of movement of a flexible floating boom in containing industrial gear oil under the combined waves and currents. Good agreements are obtained between the SPH modeling results and the experimental data in terms of the ambient wave-current field, hydrodynamic responses of the floating body and evolution process of the oil slick for the flexible boom. The hydrodynamic responses and containment performances of the flexible floating boom are also compared with those of the rigid one. It is found from both the experimental and numerical results that two vortices of the water phase exist in the front and rear of the boom skirt and the size of the front vortex decreases with an increase of the current velocity while the wake vortex is reversed. It is also found that the skirt of the flexible boom has a larger magnitude of the swaying and rolling than the rigid one and the maximum quantity of the escaped oil of a flexible boom within one wave cycle is about 5% more than a rigid one under the present test conditions.

Key words: oil spill, flexible floating oil boom, multi-body system, hydrodynamic performance, containment process, multiphase SPH model

1. INTRODUCTION

Oil spills, e.g. the Deepwater Horizon oil spill event in Gulf of Mexico on 20 April, 2010, can bring serious disasters on the marine and coastal environment as a result of both the physical smothering and the toxic effects. Floating oil booms are commonly used in concentrating the spilled oil and preventing the oil from spreading. The performance of a floating boom to contain the spilled oil is affected not only by the characteristics of itself, e.g. the floater diameter, skirt length, buoyancy/weight (B/W) ratio and boom flexibility, but also by the contained oil properties, e.g. the spilled volume, viscosity and density. The failure modes of the oil containment, such as the oil splash-over, boom submergence and overturning, mainly depend on the hydrodynamic responses of the floating oil boom, while the failure modes of drainage (Cross and Hoult, 1971; Wilkinson, 1972), entrainment (Wicks III, 1969) and critical accumulation (Delvigne, 1989;

Johnston et al., 1993) mainly happen during the evolution process of the oil-water interface in the front of boom.

Up till now, quite a number of numerical models have been proposed for revealing the relation between the capacity and behavior of oil containment of an oil boom and its mechanical characteristics under the action of combined waves and currents. An et al. (1996) and Goodman et al. (1996) investigated the oil-water flow around a stationary boom by using the commercial CFD software package FLUENT and three typical containment failure modes were successfully reproduced in their simulations, namely the drainage failure, droplet entrainment and critical accumulation. The simulated results show satisfactory agreement with the experimental data of Brown et al. (1996) in terms of the length and general thickness profiles of the oil slick. Fang and Johnston (2001) developed a more comprehensive non-hydrostatic flow model to simulate the oil contained by a stationary boom under the action of waves, currents and winds. It is found that the oil-water interface is more unstable at the upstream end of the oil slick than near the boom under the action of waves with the boom fluctuations being positively correlated with the wave height. The fluctuation of the interface induced by the waves can be suppressed due to the presence of the current. The effect of winds on the oil containment is similar to that of the currents and can be regarded as an additional current velocity (about 1~6% of the wind velocity). Violeau et al. (2007) and Yang and Liu (2013) applied the SPH model to simulating a movable oil boom interaction with the oil slick, however only heave movement of the boom was considered in their simulations and the roll and sway motions as well as the effect of flexibility of the boom were ignored. With regard to the boom flexibility, Amini et al. (2005) developed a numerical coupling model of fluid-structure interaction based on FLUENT to assess the containment process of oil boom and indicated that a flexible skirt could significantly change the pressure on the boom skirt and accordingly affect the oil containment process. Recently, Amini and Schleiss (2009) found that the wake vortex could spread over a wider range of areas behind the rigid boom than the flexible one under the current condition. The use of a rigid-lid CFD model and simplification of the boom as a thin baffle in their simulations imposed limitation on revealing some more practical mechanisms.

Comparatively, the Lagrangian meshless methods, such as the Smoothed Particle Hydrodynamics (SPH), have clear advantages in modeling complex fluid-structure interaction (FSI) problems with multi-interfaces through explicitly tracking (Yang et al., 2014; Liu and Li, 2016). A number of documented works were reported on modeling the interaction of multiphase fluids with structure by using the SPH method. Colagrossi and Landrini (2003) proposed a two-phase SPH model to simulate the violent fluid-structure interactions with air entrapment and large surface tension was incorporated in the lower-density phase for the purpose of interface stability. Hu and Adams (2006; 2007) developed a multi-phase SPH method, which can handle the density discontinuities across the phase interface naturally but the model application is mainly for the non-free surface flows. Based on the works of Colagrossi and Landrini (2003) and Hu and Adams (2006), Grenier et al. (2009) derived a Hamiltonian interface SPH formulation and simulated both interface and free surface flows. Considering the heavy computational cost for determining the volume distributions of particles in Grenier et al. (2009), Monaghan and Rafiee (2013) later proposed a relatively simpler algorithm for the multi-fluid flow with high density ratios. They found that the velocity smoothing and artificial surface tension used by Colagrossi and Landrini (2003), the number density concept adopted by Hu and Adams (2006), and the compensating functions used by Grenier et al. (2009) are not a necessity.

This paper presents a weakly compressible Smoothed Particle Hydrodynamic (WCSPH) model for the multiphase flows with complex interfaces, which is similar to that used by Monaghan and Rafiee (2013) in dealing with flow of multiphase fluids with different density. An algorithm based on the dynamic boundary particles (Dalrymple and Knio, 2001) was introduced to remove the spurious pressure oscillations near the interface of multi-fluids and the solid body. It is then combined with a Rigid Module and Flexible Connector (RMFC) approach of multi-body system (Riggs and Ertekin, 1993) to treat the flexible floating boom. Simulation of boom movement under the action of coupled wave-current is performed in consideration of three degrees of freedom including the heave, sway and roll.

The paper is organized as follows. After the introduction section, the methodology of the numerical model is presented, which includes the governing equations of the WCSPH model, the solid boundary treatment, the equations of motion of the rigid body and multi-body system, and the solution algorithm. In Section 3, the numerical model is validated against the data collected from the wave-current flume and wedge entry into a two-layer water-oil fluid. In Section 4, extensive discussions are performed in terms of the optimization of elastic coefficient of mooring line and the multi-body system, the simulation of the interaction of floating boom with the waves, and the hydrodynamic characteristics of the floating boom with different flexibilities. In Section 5, the combined effects of current, wave and boom flexibility on the oil containment failures are investigated by using the improved WCSPH model. Finally, in Section 6 the conclusions are summarized.

2. METHODOLOGY OF NUMERICAL MODEL

2.1. Governing equations

Fluid motion is governed by the mass and momentum conservation equations, expressed as:

$$\frac{\mathrm{d}\rho}{\mathrm{dt}} = -\rho\nabla\cdot\mathbf{v} \tag{1}$$

$$\frac{\mathrm{d}\mathbf{v}}{\mathrm{dt}} = -\frac{1}{\rho}\nabla \mathrm{p} + \nu\nabla^2\mathbf{v} + \frac{1}{\rho}\nabla\cdot\boldsymbol{\tau} + \mathbf{g} \tag{2}$$

where ρ denotes the density of the fluid; t the time; $\boldsymbol{v}$ the velocity vector; p the pressure and **g** the gravitational acceleration; ν the molecular viscosity of laminar flow; and $\boldsymbol{\tau}$ the sub-particle-scale (SPS) turbulence stress tensor.

In the SPH approach, the fluid is assumed to be weakly compressible and the pressure is determined via an equation of state (Monaghan and Kos, 1999), written as follows:

$$\mathrm{p} = \frac{\mathrm{c}_0^2\rho_0}{\gamma}\left[(\rho/\rho_0)^{\gamma} - 1\right] \tag{3}$$

where c_0 denotes the sound speed at the reference density and is evaluated to keep the relative density fluctuation being less than 0.01; ρ_0 the reference density; and $\gamma = 7.0$.

In order to close the governing equations, the eddy viscosity assumption (Boussinesq's hypothesis) is used to model the SPS turbulence stress (Gotoh et al., 2001):

$$\frac{\boldsymbol{\tau}_{\mathrm{ij}}}{\rho} = \nu_{\mathrm{t}}\left(2\mathrm{S}_{\mathrm{ij}} - \frac{2}{3}\mathrm{k}\delta_{\mathrm{ij}}\right) - \frac{2}{3}\mathrm{C}_{\mathrm{I}}\Delta^2\delta_{\mathrm{ij}}\left|\mathrm{S}_{\mathrm{ij}}\right|^2 \tag{4}$$

where $\boldsymbol{\tau}_{ij}$ denotes the sub-particle scale stress tensor; $\nu_t = [C_s\Delta l]^2|S|$ the turbulence eddy viscosity; k the SPS turbulence kinetic energy; C_s the Smagorinsky constant, ranging in 0.1-0.24 (Rogallo and Moin, 1984), and is evaluated by 0.12 in the present study; Δl the filter length and $|S_{ij}|=(2S_{ij}S_{ij})^{1/2}$, where S_{ij} the component of SPS strain tensor; C_I a constant with value of 0.0066; and δ_{ij} the Kronecker delta.

Note that the same equation of state is used for the different fluid phases while different values of the sound speed and reference density should be adopted for each phase. According to Violeau et al. (2007), the above equations can hold as long as the density ratio of two phases of the fluid is less than 2. Monaghan and Rafiee (2013) further proposed that the speed of sound in the lighter fluid was generally greater than that of the denser one. As for the density ratio of multi-phase fluids in the range of 1 - 2, very satisfactory results have been obtained for the ratio of sound speed being equal to 1. Thus the sound speed of both the oil and water used in the present study is taken as 10 times the estimated maximum fluid velocity.

By following the SPH approach of Lo and Shao (2002), Yang and Liu (2013) and Monaghan and Rafiee (2013), Eqs. (1) and (2) are discretized by using the kernel approximation as:

$$\frac{\mathrm{d}\rho_\mathrm{i}}{\mathrm{dt}} = \sum_{\mathrm{j}\subset \mathrm{A}} \mathrm{m_j} \mathbf{v}_\mathrm{ij} \cdot \nabla_\mathrm{i} \mathrm{W_{ij}} + \rho_\mathrm{i} \sum_{\mathrm{j}\not\subset \mathrm{A}} \mathrm{V_j} \mathbf{v}_\mathrm{ij} \cdot \nabla_\mathrm{i} \mathrm{W_{ij}} \tag{5}$$

$$\frac{\mathrm{d}\mathbf{v}_\mathrm{i}}{\mathrm{dt}} = -\sum_\mathrm{j} (1+\mathrm{R_{ij}}) \mathrm{m_j} \left(\frac{\mathrm{p_i}}{\rho_\mathrm{i}^2} + \frac{\mathrm{p_j}}{\rho_\mathrm{j}^2} \right) \nabla_\mathrm{i} \mathrm{W_{ij}} + \sum_\mathrm{j} \mathrm{m_j} \left(\frac{4\nu_0 \mathbf{r}_\mathrm{ij} \nabla_\mathrm{i} \mathrm{W_{ij}}}{\bar{\rho}_\mathrm{ij} \left| \mathbf{r}_\mathrm{ij} \right|^2} \right) \mathbf{v}_\mathrm{ij} + \sum_\mathrm{j} \mathrm{m_j} \left(\frac{\boldsymbol{\tau}_\mathbf{i}}{\rho_\mathrm{i}^2} + \frac{\boldsymbol{\tau}_\mathbf{j}}{\rho_\mathrm{j}^2} \right) \nabla_\mathrm{i} \mathrm{W_{ij}} + \mathbf{g}_\mathrm{i} \tag{6}$$

where subscript i denotes the index of the target particle and subscript j the index of the neighboring particle within the compact support of i; subscript $\mathrm{j} \subset \mathrm{A}$ means that both particles i and j are from the same fluid phase while $\mathrm{j} \not\subset \mathrm{A}$ indicates the other way; m_j the mass of particle; V_j the volume of particle; $\rho_{ij}=0.5(\rho_i+\rho_j)$, $\boldsymbol{v}_{ij}=\boldsymbol{v}_i-\boldsymbol{v}_j$, $\mathbf{r}_{ij}=\mathbf{r}_i-\mathbf{r}_j$.

Besides, the repulsive force is incorporated into the fluids of different types, and the multiphase repulsive force coefficient R_{ij} in Eq. (6) can be approximated by (Monaghan and Rafiee, 2013)

$$\mathrm{R_{ij}} = \begin{cases} 0.08\left(\dfrac{\rho_\mathrm{w} - \rho_\mathrm{o}}{\rho_\mathrm{w} + \rho_\mathrm{o}} \right), & \mathrm{j} \not\subset \mathrm{A} \\ 0, & \mathrm{j} \subset \mathrm{A} \end{cases} \tag{7}$$

where ρ_w denotes the density of sea water; and ρ_o the density of spilled oil. As mentioned in Monaghan and Rafiee (2013), a small (<8%) increase in the pressure term is found when the interaction takes place between the particles from different fluids. Here it should be mentioned that the interface tension also plays an important role when the unstable interfacial wave occurs. In the present paper, however, we just consider the effect of the density and viscosity of the fluid, while ignore the surface tension force, since the research is focused on the containment performance of the floating boom with different skirt stiffness but not the leaking process of the oil droplets.

Here a quintic kernel function W_{ij} suggested by Wendland (1995) is adopted:

$$W_{ij} = \frac{7}{4\pi h^2}\begin{cases}\left(1-\frac{q}{2}\right)^4(2q+1), & 0 \le q < 2 \\ 0, & q \ge 2\end{cases} \tag{8}$$

where q=$\triangle r_{ij}$ /h, $\triangle r_{ij}$ the distance between particles i and j; and h the smoothing length and usually taken as 1.3 times of the initial particle spacing in consideration of the particle configuration of the floating boom.

To overcome the high frequency fluctuations of the pressure field, the zeroth order Shepard filter (Dalrymple and Rogers, 2006) is applied to the whole set of fluid particles once every 20 time steps to correct the fluid density field, written as:

$$\tilde{\rho}_i = \sum_{j \subset A} m_j \frac{W_{ij}}{\sum_j \frac{m_j}{\rho_j} W_{ij}} \tag{9}$$

Note that the above density filter is applicable only to the case that the density ratio of multi-phase flows is low, e.g. less than 2 as the case of present study, and should be applied only to the particles within the same fluid phase. As for the multiphase flows with high density ratio, a revised form of this equation must be used (Chen et al., 2015).

The motion of particles are governed by the XSPH variant (Monaghan, 1989), where X is an indication of unknow factor

$$\frac{d\mathbf{x}_i}{dt} = \mathbf{v}_i - \varepsilon \sum_j \frac{m_j}{\bar{\rho}_{ij}} \mathbf{v}_{ij} W_{ij} \tag{10}$$

where ε is taken as 0.2~0.4, and the second term on the right hand side of Eq. (10) contributes to driving the particle i with a velocity being closer to the average value of its neighboring particles for reducing the particle disorder.

2.2. Boundary condition treatment

Due to that the continuous density method is adopted to update the particle density, the free surface conditions are automatically satisfied by the mesh-free nature of SPH and no special boundary conditions are imposed on the free surface particles. The solid boundary is described by the double rows of the Dynamic Boundary Particles (DBPs) by following Crespo et al. (2007) and Ren et al. (2015). The DBPs have the same attributes as the fluid particles in that they must satisfy the governing equations of continuity, momentum and the state equation, while they do not follow the updating of the XSPH variant Eq. (10).

2.2.1 Wave-current flume

The particles to form the wave generator are forced to move in accordance with the solution of wave propagation and the active wave absorption correction, expressed as follows:

$$\mathbf{v}_{\mathrm{wm}} = \frac{\partial \mathbf{X}_{\mathrm{wm}}}{\partial \mathrm{t}} = \frac{\omega}{\mathrm{Q}}\left[2\eta - \eta_{\mathrm{wm}}\right] \tag{11}$$

where $\mathbf{v}_{\mathrm{wm}}$ and $\mathbf{X}_{\mathrm{wm}}$ denote the temporal velocity and displacement of wave generator; η= Hsin(ωt)/2 the temporal free water surface elevation, H the target wave height; ω the target wave frequency; η_{wm} the measured instantaneous water surface elevation in the vicinity of the wave generator; and Q the hydrodynamic transfer function given by Hirakuchi et al. (1990), expressed as

$$\mathrm{Q} = \frac{4\sinh^2(\mathrm{kd})}{2\mathrm{kd} + \sinh(2\mathrm{kd})} \tag{12}$$

where k denotes the wave number and d denotes the depth of water in the flume.

The numerical wave-current flume is set up by following Klopman's experiment (1994). The current circulation is implemented by building an inlet and outlet on the bottom of the flume (Fig. 1) and applying the periodical boundary condition to the boundary area. The velocity of the particles inside the inlet and outlet boundary areas is forced to satisfy the specified discharge.

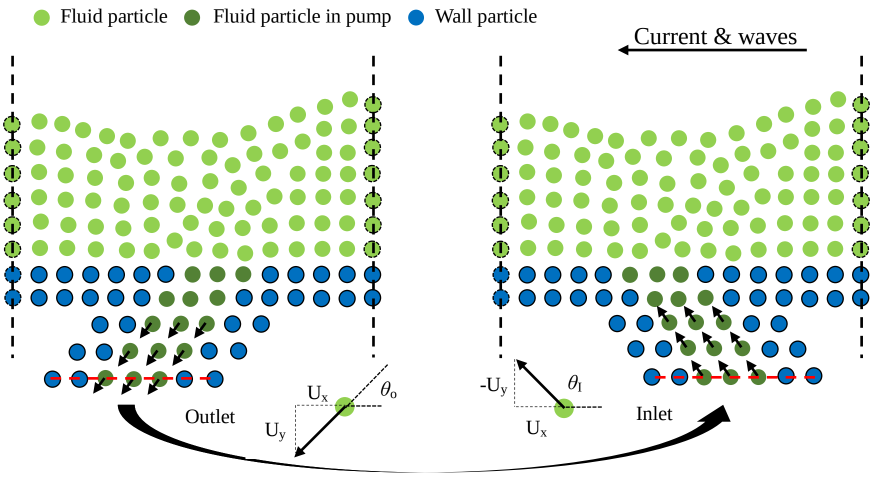

Fig. 1. Sketch of numerical wave-current flume. U_x and U_y denote the horizontal and vertical component of particle velocity, θ_I and θ_o the degree of the inflow and outflow at the inlet and outlet with respect to the horizontal direction.

2.2.2 Particle filter

To suppress the unrealistic pressure fluctuations around the cross-point of the two-fluid phase interfaces and the solid boundary, the particle filtering based on Ren et al. (2015) is performed over all the solid boundary particles for their density, pressure and mass (Fig. 2), which is expressed as

$$\tilde{\Phi}_i = \chi \Phi_w + (1-\chi)\Phi_o \tag{13}$$

where χ denotes the volume fraction of water phase within its compact support; Φ_w and Φ_o the volumetric average of physical quantities in the water and oil phase, respectively. The essential difference of the boundary treatment between Ren et al. (2015) and the present model is that the particle mass of all the Dynamic Boundary Particles (DBPs) is updated on the basis of the distribution of neighbour fluid particles in our approach, while the particle mass is not updated in the algorithm of Ren et al. (2015). When the solid boundary particles are surrounded by only one fluid phase, the relevant physical quantities of the DBPs are determined only from the particles of this fluid phase.

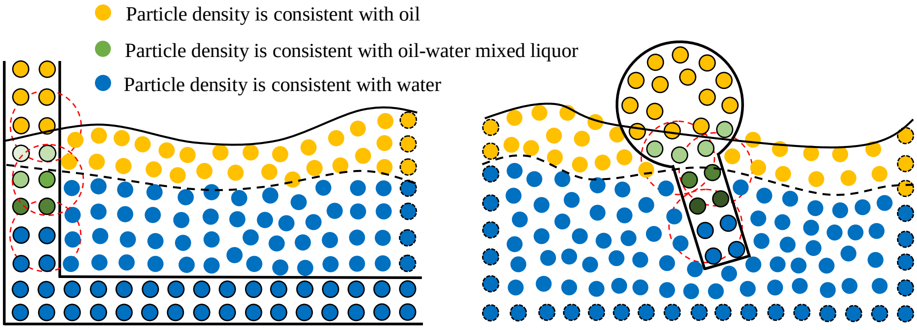

Fig. 2. Sketch of solid boundary treatment (Different colors distinguish the particles with different masses): DBPs in the water flume (left); DBPs of the simplified floating boom (right).

Movement of a floating body is determined from the rigid body dynamics. The forces exerted on the surface particles of the floating body can be calculated by the volume integration of the fluid stresses of all the surrounding fluid particles within the compact support as

$$\mathrm{f}_\mathrm{i} = \tilde{\mathrm{m}}_\mathrm{i}\left[-\sum_\mathrm{j}\mathrm{m}_\mathrm{j}\left(\frac{\tilde{\mathrm{p}}_\mathrm{i}}{\tilde{\rho}_\mathrm{i}^2}+\frac{\mathrm{p}_\mathrm{j}}{\rho_\mathrm{j}^2}\right)\nabla_\mathrm{i}\mathrm{W}_\mathrm{ij}+\sum_\mathrm{j}\mathrm{m}_\mathrm{j}\left(\frac{4\tilde{\nu}_0\mathbf{r}_\mathrm{ij}\nabla_\mathrm{i}\mathrm{W}_\mathrm{ij}}{\bar{\rho}_\mathrm{ij}\left|\mathbf{r}_\mathrm{ij}\right|^2}\right)\mathbf{v}_\mathrm{ij}+\sum_\mathrm{j}\mathrm{m}_\mathrm{j}\left(\frac{\tilde{\boldsymbol{\tau}}_\mathbf{i}}{\tilde{\rho}_\mathrm{i}^2}+\frac{\boldsymbol{\tau}_\mathbf{j}}{\rho_\mathrm{j}^2}\right)\nabla_\mathrm{i}\mathrm{W}_\mathrm{ij}+\mathbf{g}_\mathrm{i}\right] \tag{14}$$

where $\tilde{\mathrm{m}}_\mathrm{i}$, $\tilde{\mathrm{p}}_\mathrm{i}$, $\tilde{\rho}_\mathrm{i}$, $\tilde{\boldsymbol{\tau}}_\mathrm{i}$, $\tilde{\nu}_0$ denote the corrected mass, pressure, density, stress tensor and molecular viscosity of the boundary particle, respectively. Since a mixed form of the continuity equation [Eq. (5)] proposed by Yang and Liu (2013) is used in the present study, whose first term on the right-hand-side contains the particle mass of the ambient fluid particles and DBPs, inconstant mass can be resulted for the particles of the floating body. This treatment may in certain degree lead to non-conservation of the mass and consequently the momentum in the ambient fluid particles. Nevertheless, no unusual phenomena was observed on the fluid particles around the structure. Therefore the treatment can be thought as acceptable.

2.3. Approach for motion of flexible floating boom

The motion of a rigid floating boom is governed by the dynamic equations of the translational and rotational movement, written as

$$\mathrm{M}\frac{\mathrm{d}\mathbf{V}}{\mathrm{dt}} = \sum_{\mathrm{i}\subset\mathrm{DBPs}} \mathbf{f}_{\mathrm{i}} + \mathrm{M}\mathbf{g} \tag{15}$$

$$\mathrm{I}\frac{\mathrm{d}\boldsymbol{\Omega}}{\mathrm{dt}} = \sum_{\mathrm{i}\subset\mathrm{DBPs}} \left(\mathbf{r}_{\mathrm{i}} - \mathbf{R}_0\right) \times \mathbf{f}_{\mathrm{i}} \tag{16}$$

where M and I denote the mass and inertia moment of the floating boom, respectively; $\mathbf{V}$ and $\boldsymbol{\Omega}$ the linear and angular velocity of the floating boom, respectively; $\mathbf{f}_\mathrm{i}$ the total forces exerting on the moving solid boundary particle; and $\mathbf{R}_0$ the position vector of the mass center of the floating boom.

Then the velocities of the particles on the floating boom can be solved from

$$\frac{\mathrm{d}\mathbf{r}_{\mathrm{i}}}{\mathrm{dt}} = \mathbf{V} + \boldsymbol{\Omega} \times \left(\mathbf{r}_{\mathrm{i}} - \mathbf{R}_0\right) \tag{17}$$

Being different from the rigid boom, the flexible floating boom is simulated by a multi-body system (Fig. 3), in which the whole boom is separated into several RMFCs (Riggs and Ertekin, 1993). Each module has three degrees of the freedom for a two-dimensional space, i.e. heave, sway and roll. All deflections of the skirt come from the flexible connectors.

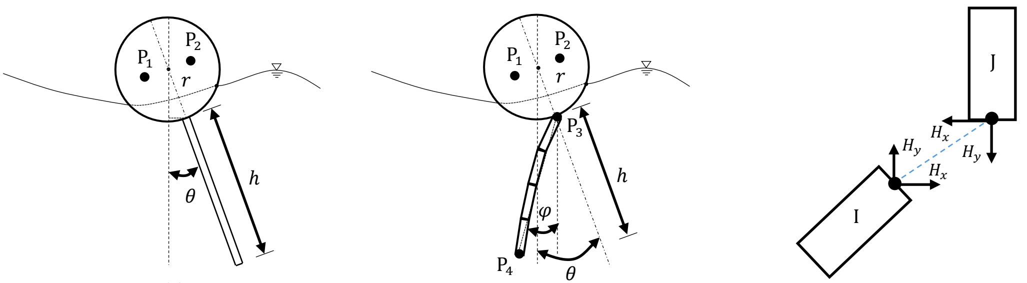

(a) (b) (c)

Fig. 3. Schematic view of oil boom section: (a) Rigid boom in motion; (b) Flexible boom in motion; and (c)

Detailed drawing of skirt section. r denotes the floater radius, h the projection length of the skirt on the vertical symmetry axis of the structure, θ and φ the rolling angle of the floater and the skirt, positive in the clockwise direction, I and J the adjacent skirt modules, and H_x and H_y the horizontal and vertical component of hinge force. P_1~P_4 denotes the tracer points on the boom model to record the boom motion.

The position of each module is separately updated via solving Eqs. (15) and (16), in which the forces $\mathbf{f}_i$ exerted on each floating boom particle consist of the fluid force $\mathbf{f}_{fi}$, mooring force $\mathbf{f}_{mi}$ and hinge force $\mathbf{f}_{hi}$ expressed as:

$$\mathbf{f}_i = \mathbf{f}_{fi} + \mathbf{f}_{mi} + \mathbf{f}_{hi} \tag{18}$$

The mooring force $\mathbf{f}_{mi}$ can be written as

$$\mathbf{f}_{mi} = \begin{cases} k_t \mathbf{l}_{i0} & \left|\mathbf{f}_{mi}\right| > 0 \\ 0 & \left|\mathbf{f}_{mi}\right| \le 0 \end{cases} \tag{19}$$

where k_t denotes the coefficient of elasticity of the mooring line; and $\mathbf{l}_{i0}$ the length increment vector of the mooring line.

The connectors are modeled by a linear, translational and ‘zero-length’ spring (Riggs et al., 1998) and no rotational stiffness is incorporated. The hinge forces between the two skirt modules are equal in magnitude but opposite in direction and can be obtained from a force-displacement relation, written as

$$\mathbf{f}_{hi} = k_h \mathbf{r}_{ij} \tag{20}$$

where k_h denotes the translational stiffness of the connector; and $\mathbf{r}_{ij}$ the relative displacement vector between the two adjacent connectors of module I and J (Fig. 3).

2.4. Solution algorithm

The predictor-corrector algorithm is adopted for time-stepping of the present SPH model (Monaghan, 1989). The total fluid force on the floating body is obtained by summing up the force of each particle calculated from Eq. (14). The velocity and position of the wave generator and floating body are updated by solving Eqs. (11), (15) and (16). The computational time step is adjusted by satisfying the Courant condition, according to Monaghan and Kos (1999).

3. MODEL VALIDATION AND RESULT ANALYSIS

3.1. Validation of velocity profiles of numerical wave-current flume

The validity of the numerical model is firstly proved by comparison of the modeled results of velocity profiles of a numerical wave-current flume against the experimental data of Klopman (1994). The numerical wave-current flume is 20 m long with initial water depth of 0.5 m. A flow circulation system is established to provide a constant discharge of Q ≈ 80 l/s. The distance between the inlet and the left end and between the outlet and the right end of the flume is about 1.5 times the wave length. The inflow direction and outflow direction at the inlet and outlet are set at 45 degree and 135 degree (Fig. 4), respectively, with respect to the horizontal direction for smooth divergence and confluence of the current and wave flows. The inner diameter of the inlet and the outlet is set as 0.3 m. A sponge layer with linear damping is placed at the right end of the flume for wave absorption. The initial particle spacing is 0.02 m for all kind of particles (solid or fluid) and approximately 25200 water particles and 2264 solid particles are employed in the computation. The code is parallelized using the OpenMP formalism to reduce the execution time of the simulations. A workstation (Model PR4840R from PowerLeader, Inc.) with four octa-core Intel Xeon E5-4620v2 processors (clock speed of 2.6 GHz and 256.0 GB RAM) is used to carry out all the simulations. Taking this case for example, it takes around 1 day 3 h CPU time to complete a simulation of time period 200 s.

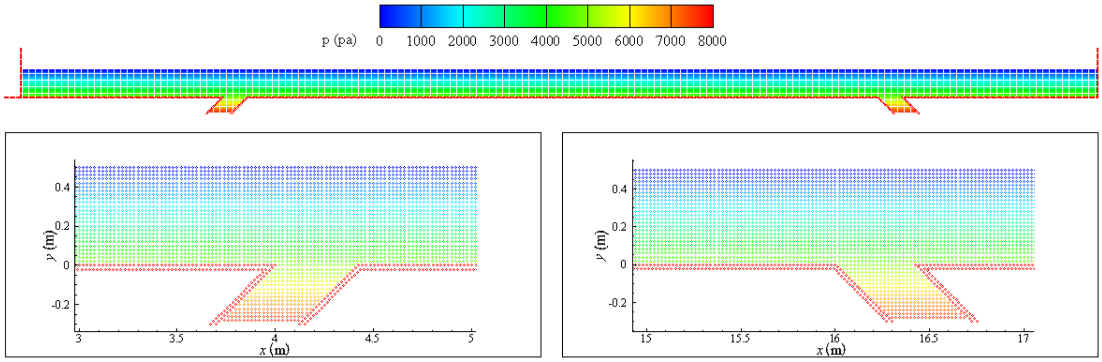

Fig. 4. Initial configuration of wave-current flume: flume setup with fluid particles colored by hydrostatic pressure (top); close-up view of the configuration of inlet (left); close-up view of the configuration of outlet (right).

The calculated results of the vertical profile of horizontal velocity for the cases of both current alone and wave-following-current are in good agreement with the measured results despite of some slight overestimations at the middle of the water column (Fig. 5).

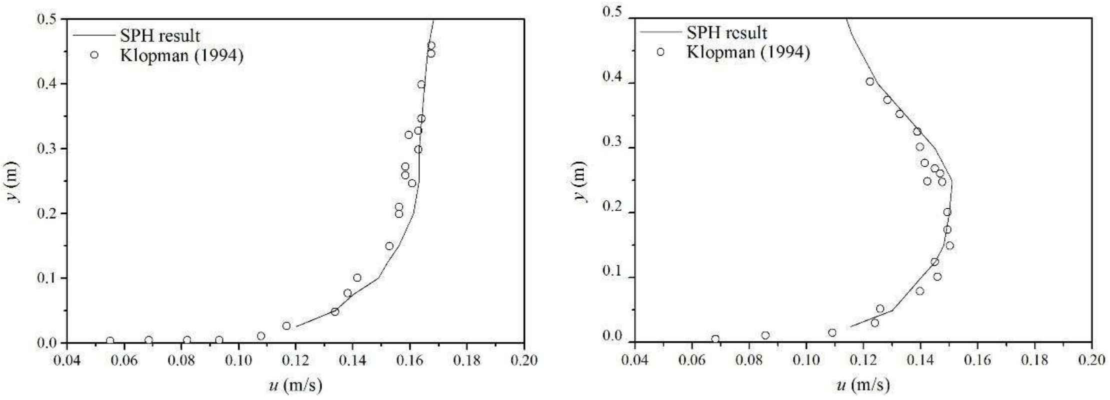

Fig. 5. Vertical profiles of the mean horizontal velocity: for current alone (left); for waves (H=0.12 m, T=1.4 s) following current (right).

3.2. Validating wedge falling into multi-fluid

To examine the effect of particle filtering for the simulation of interaction between the multi-phase fluids and the moving rigid body involving violent multi-interface deformation, an experiment of wedge falling into calm two-layer water-oil fluid is carried out by following Gong et al. (2016).

Fig. 6 shows the site snapshot and the schematic setup of the water tank and the falling wedge.

The glass tank is 0.4 m long, 0.2 m wide and 0.25 m high, with water layer thickness of 0.1 m and oil layer thickness of 0.05 m. Corn oil is used for the test, with the physical properties being shown in Fig. 7. The molecular viscosity and reference density of corn oil are taken as 70 mm^2/s and 848 kg /m^3, respectively, and those for the water are taken as 1 mm^2/s and 1000 kg /m^3, respectively. The wedge is made of acrylic glass and is filled with sand to obtain a weight of 0.2 kg. It is shaped as a triangular prism with the right-angle side length being 0.03 m and the dead-rise angle being 45°. The length of the wedge is 0.19 m, which is a little bit shorter than the tank width to avoid getting stuck during the falling process. The wedge was released from a distance of 0.01 m above the oil-air interface. The falling process of the wedge was recorded by a video camera. The dimension of the numerical model is the same as the physical experiment. The initial particle spacing is taken as 0.001 m for all the particles. The whole computational domain is modeled by using 2460 solid particles, 43491 water particles and 22344 oil particles. The simulated time of 0.6 s costs nearly 3 h of CPU time by using the same specification of the desktop.

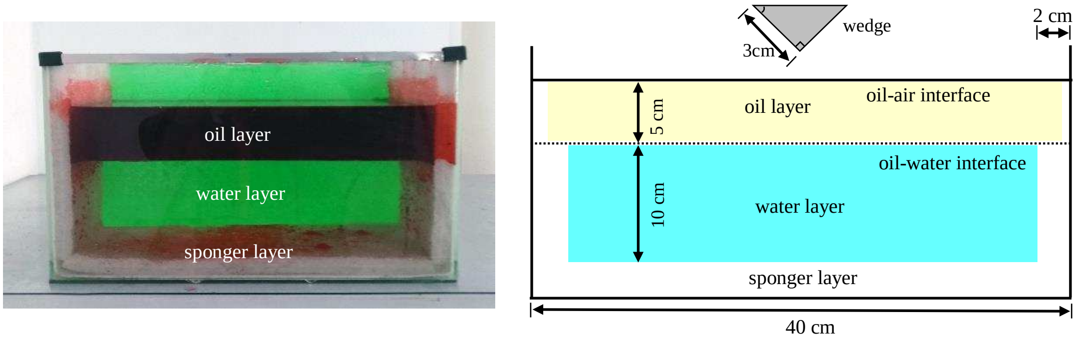

Fig. 6. Water tank and falling wedge used in the laboratory experiment: site snapshot (left); schematic view (right).

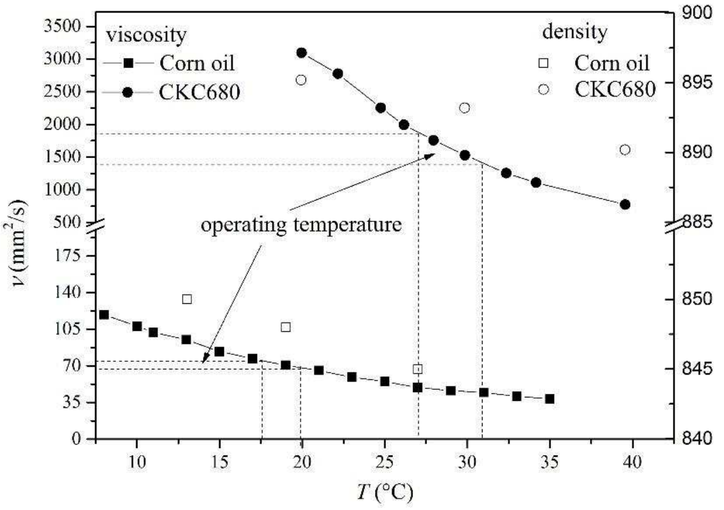

Fig. 7. Test oil properties. ν denotes the kinematic viscosity, ρ the density, and T the temperature.

To absorb the disturbance on the wall boundary, sponge layers were placed along the lateral and bottom boundary of the tank with a thickness of about 0.02 m (Fig. 6). The density of the fluid particles within the sponge layer is updated by the following formula (Gong et al., 2016):

$$\rho^{n+1} = \rho^{n} + \lambda \frac{D\rho^{n}}{Dt} \Delta t \tag{21}$$

where the wave absorption coefficient λ takes the form of

$$\lambda = 1 - a^{-0.9b\xi} \tag{22}$$

where a and b are the constants with value of 9 and 50, respectively; ξ denotes the relative coordinate inside the sponge layer, expressed as $\xi = |y_p - y_w| / l_s$, where l_s denotes the width of the sponge layer, y_p the coordinate of fluid particles, and y_w the coordinate of inner surface of the sponge layer.

As a heavy wedge was adopted in the test, the wedge would maintain straight downward trajectory with no side rotations during the falling process, and the horizontal force and overturning moment exerting on the wedge are in balance. In the numerical simulation, however, due to the spurious numerical oscillation of the pressure, penetration of the water particles across the water-solid interface may happen if the particle filtering process is not adopted in the SPH model (Fig. 8), which will lead to the particle disorder and horizontal fluctuating force and overturning moment. The maximum amplitude of the oscillation of the horizontal force can be as high as 100 $\mathrm{kg \cdot m/s^2}$ and the maximum overturning moment can be up to 1.5 $\mathrm{kg \cdot m^2/s^2}$ (Fig. 8). However, this can be overcome effectively by applying the particle filter on the DBPs (Fig. 8 as well). Fig. 9 (right) shows that after using the particle filter, the fluid particles are more equally spaced in the vicinity of the wedge without any unphysical separation and penetration (left) and therefore no disturbance is observed in the ambient pressure field.

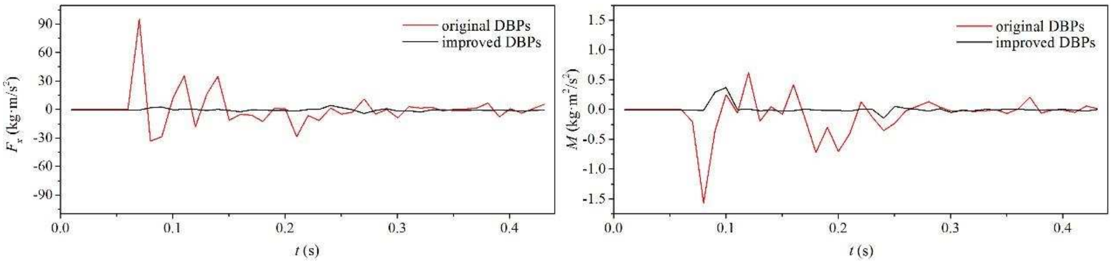

Fig. 8. Horizontal force F_x (left) and overturning moment M (right) in the process of wedge entry using original and improved DBPs.

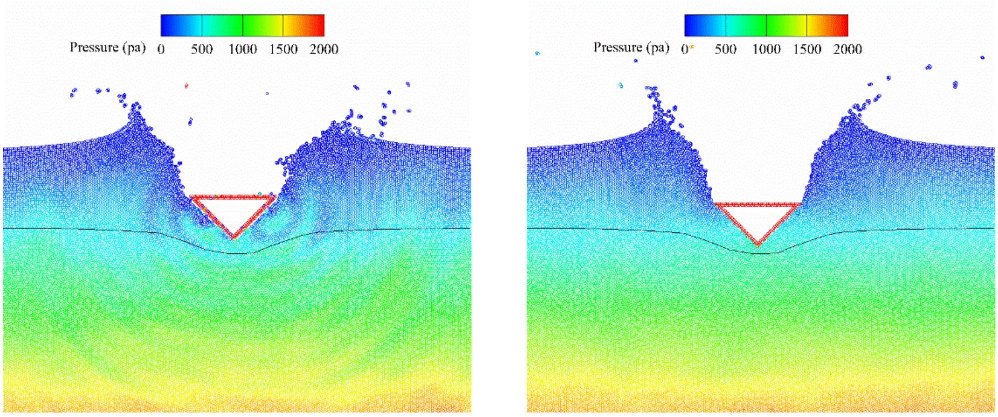

Fig. 9. Particle snapshots of wedge entry at time t = 0.15 s (black lines denote the oil-water interface): original DBPs (left); and improved DBPs (right).

Fig. 10 shows the good agreement of the modeled positions of the falling wedge and the ambient fluid movement with the observed results of the experiment. The wedge firstly plunges into the water surface with a violent splashing of the water jet. A slightly bulging oil-water interface beneath the wedge suggests the effects of pressure wave resulted from the slamming of water entry [Fig. 10 (a)]. The above phenomena become more apparent with more parts of the wedge immersed into the water till the wedge comes into contact with the oil-water interface [Fig. 10 (c)]. Hereafter, the falling wedge continuously passes through the oil-water interface and sinks into the oil layer completely [Fig. 10 (d)]. This process is accompanied by the density transition of the particles consisting the wedge from the oil to the water [Figs. 10 (c) - (d)].

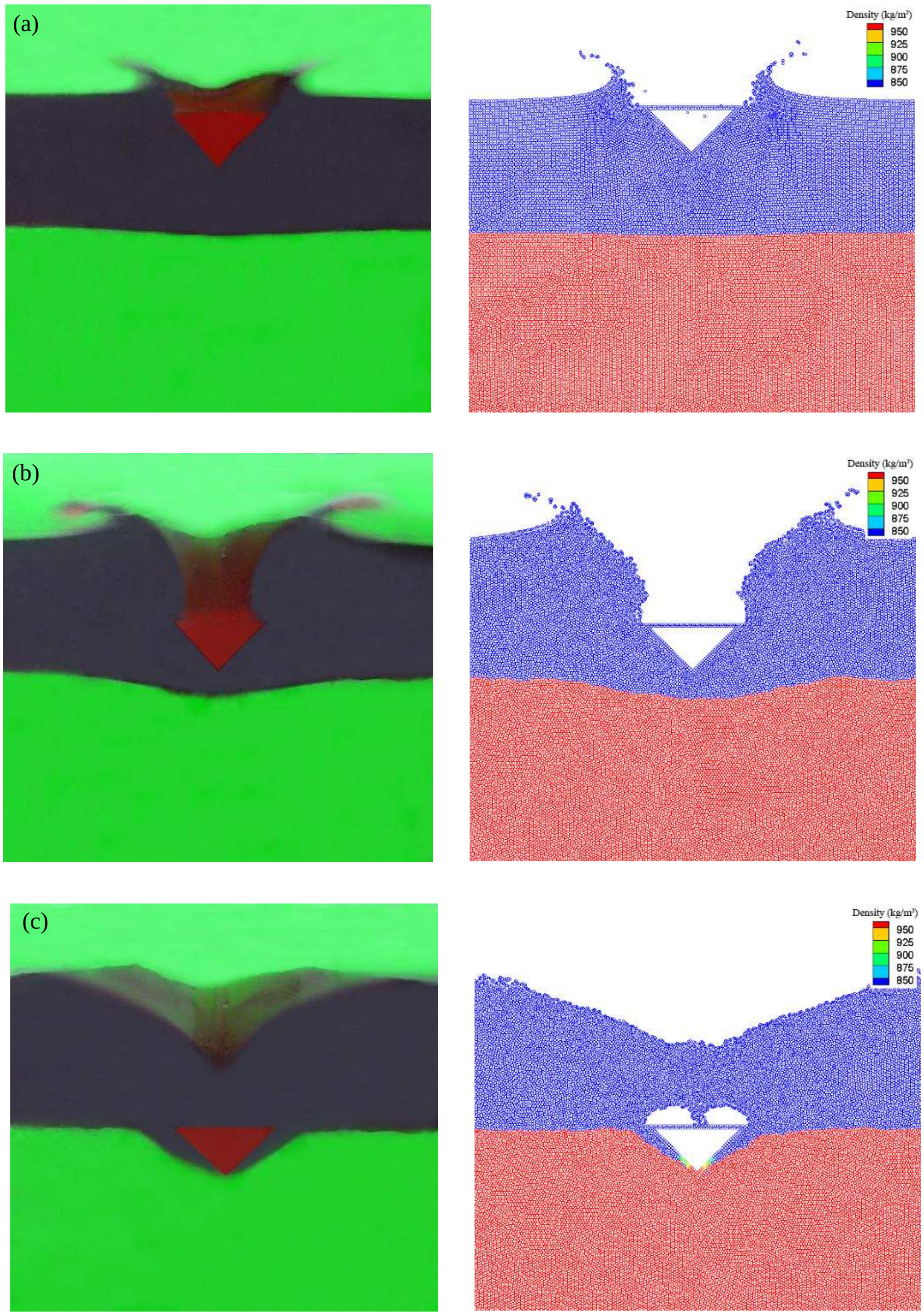

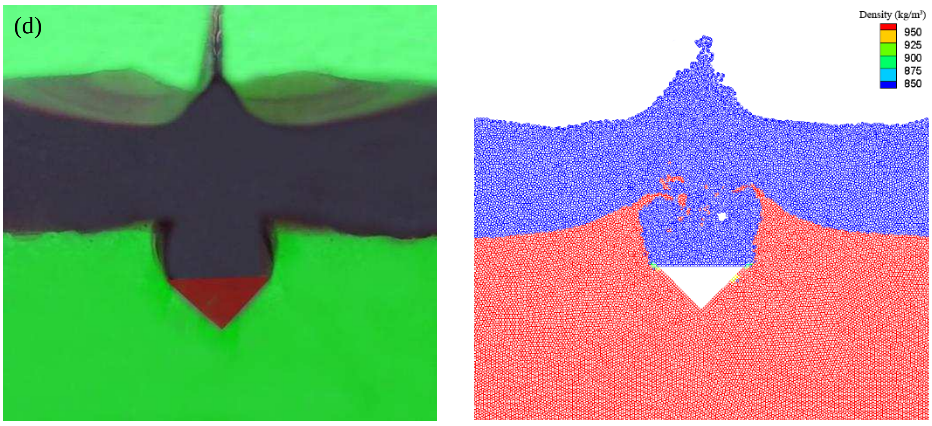

Fig. 10. Comparisons between experimental photo (left) and modeled results (right) of wedge entry across air-oil and oil-water interface: (a) $t_1 = 0.08$ s, (b) $t_2 = 0.16$ s, (c) $t_3 = 0.24$ s and (d) $t_4 = 0.36$ s.

To further investigate the accuracy of the proposed multiphase WCSPH model, a comparison between the modeled and measured results of the velocity and trajectory of the falling wedge is given. It can be seen in Fig. 11 that despite the small discrepancy between the simulated and the experimental results, they are in the same phase. The velocity of the falling wedge firstly increases and then decreases till the time instant t = 0.24 s. At this moment, the wedge begins to fall across the oil-water interface, after which the wedge keeps falling inside the water layer at a constant speed about 0.15 m/s.

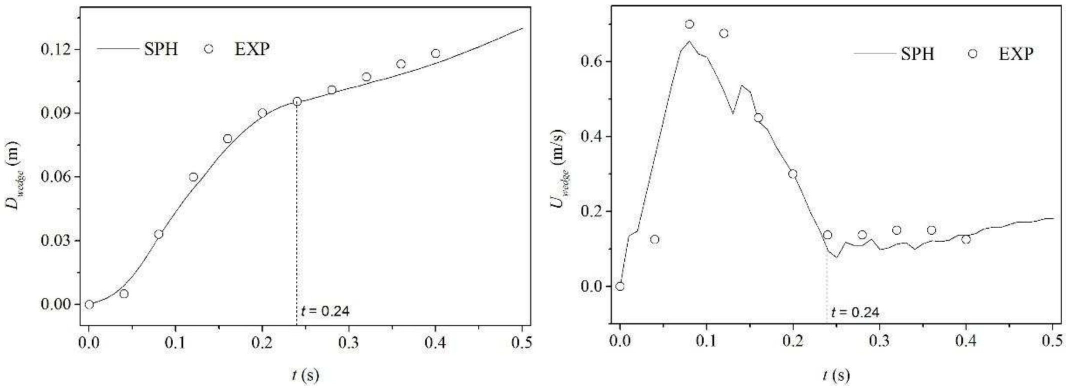

Fig. 11. Comparisons between experimental data and model results of the falling displacement D_{wedge} (left) and velocity U_{wedge} (right) of the wedge.

4. MODEL APPLICATION I: INTERACTION BETWEEN FLOATING BOOM AND COUPLED WAVES AND CURRENTS

Prior to the numerical investigation, a series of experiments were carried out in the wave-current flume of Tianjin Research Institute for Water Transport Engineering (TIWTE), Ministry of Transportation of China. The modeled results of the water surface elevation and motions of the floating boom by using the SPH model will be compared with the experimental data to verify the model, which is then applied to the evaluation of hydrodynamic performances of the floating boom focusing on the differences between the flexible skirt and the rigid one.

4.1. Experiment setup

The laboratory flume is 45 m long and 0.5 m wide. A piston-type wave generator is installed on the right-hand end of the flume and a wave absorber is placed on the opposite end of the flume. A pump is utilized to generate a steady current through a circulation system. The floating boom is restricted at the middle of the flume ($x = 0.0$ m) by two elastic mooring lines, which are attached to the joint of the floater and skirt to allow the heave, sway and roll motions in a two-dimensional frame under the action of coexisting wave-current (Fig. 12). The floating boom consists of a cylindrical floater, a skirt with stirrup to adjust its material stiffness and a counter weight on the bottom of the skirt (Fig. 13). Hair felts were used to prevent the lateral leakage of the test oil.

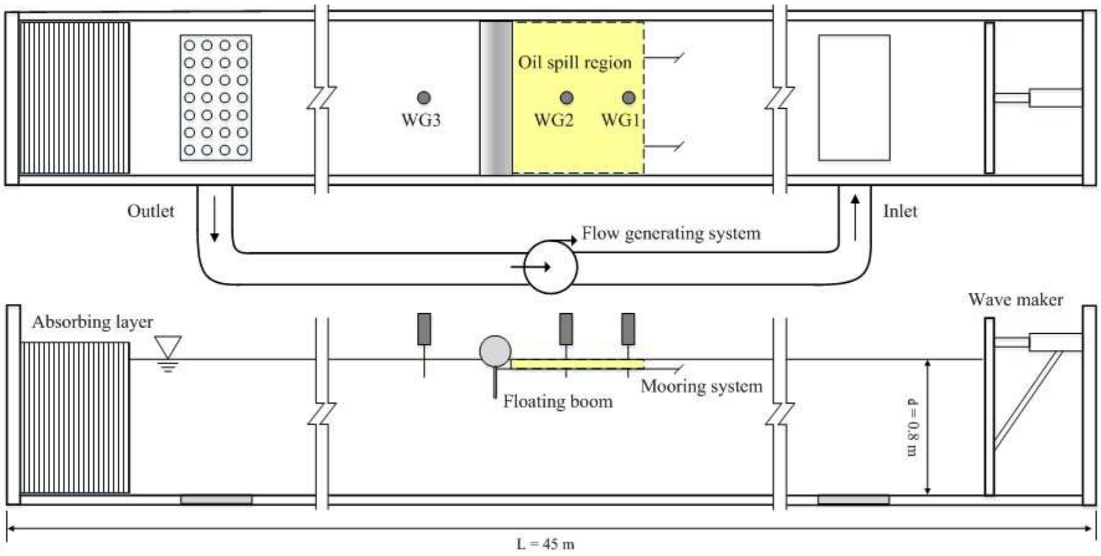

Fig. 12. Sketch of the experimental setup: top view (top); front view (bottom).

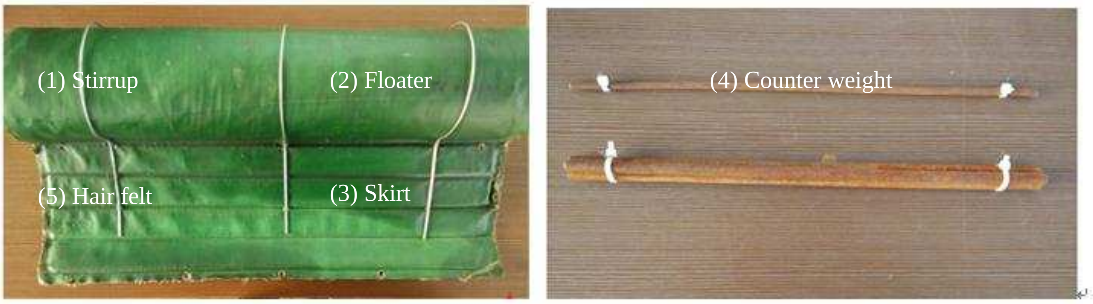

Fig. 13. Schematic view of oil boom components.

The dimensions of the boom model used in the experiment are basically the Froude scaling result of real-size oil floating boom as suggested in ASTM Standards (2013). The ratio of the model to prototype length is 1:6. The floater diameter, skirt length and skirt thickness of the rigid and flexible boom models have the same size as 0.1 m, 0.1 m and 0.005 m, respectively. The skirt of the flexible boom consists of 4 modules connected by freely-rotating connectors (Fig. 14). Each skirt module is a rigid rectangular slab with a height of 0.025 m and the centroids of each skirt module coincide with its geometric center except that the most bottom one is affected by a steel bar as the counter weight with its mass being 1.2 kg/m and diameter being 0.0012 m. The hydrodynamic effect of the steel bar is not simulated separately and both its mass and inertia moment are assigned to the bottom skirt module #4 (Fig. 14). Other parameters of the floating booms are listed in Table 1. The water depth was kept 0.8 m throughout all the test cases.

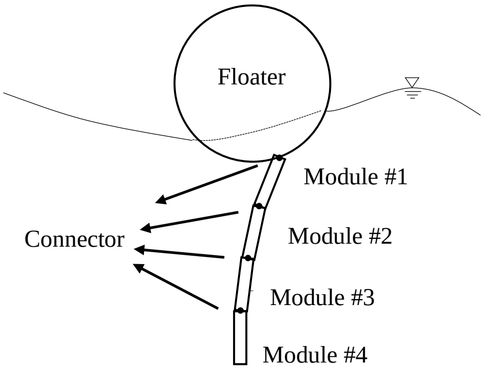

Fig. 14. Schematic view of the flexible floating boom section.

Table 1. Model boom parameters (Z denotes displacement with reference to the initial centroid of floater, and Z is positive up-wards).

Model	Component	Mass, M (kg)	Inertia moment, I (kg· m^2)	Relative position of mass center , Z (m)
Rigid	Whole	1.988	5.340×10^{-3}	-1.228×10^{-1}
	Floater	0.200	0.250×10^{-3}	0
	Module #1	0.149	7.740×10^{-6}	-6.245×10^{-2}
	Module #2	0.149	7.740×10^{-6}	-8.742×10^{-2}
	Module #3	0.149	7.740×10^{-6}	-1.124×10^{-1}
	Module #4	1.349	8.620×10^{-5}	-1.546×10^{-1}

A computer vision system (Model DS-2CD3T45D-I5 from HIKVISION, Inc.) with resolution of 2048 × 1536 pixels and frame rate 25 fps was used to capture the real-time digital images of the motions of the floating boom and the ambient water surface. The camera was fixed at about 6.0 m away from the flume sidewall and focused on a square area sized by 2.5 m×0.9 m. Green cellophane was glued on the opposite side wall of the flume to enhance the air-water contrast and to reduce the light reflection.

4.2. Numerical model setup

The computational domain of the numerical flume is set as 10.0 m long in consideration of both the computational accuracy and efficiency (Fig. 15). The floating boom is placed in the middle of the flume. Considering the resolution of the skirt, the initial particle spacing is set as 0.005 m. For the case of rigid boom, totally 328521 particles are employed in the computation, including 5298 solid particles and 323223 water particles. The rigid boom is simulated by 161 solid particles [Fig.15 (left)]. For the case of flexible boom, totally 328537 particles are employed in the computation, including 5314 solid particles and 323223 water particles. The floater of the flexible boom totally has 121 particles and each skirt module of the flexible floating boom has 14 particles [Fig.15 (right)]. The size of both the rigid and flexible boom in the numerical model is identical to that of the physical model. The simulation time is set as 20 s and the computational CPU time is nearly 2 days 17 h.

The discrete mass of the connector particles m_i is forced to be zero to avoid uneven repulsions with the ambient water particles in the computation. The mass and inertia moment of the floater and skirt are set the same as the physical ones (Table 1). The particles of the mooring lines are only used for the visualization purpose and are not involved in the SPH computations. The incident wave height is $H = 0.06$ m, and the wave period is $T = 1.2$ s. The mooring line is kept in a slight tension state by imposing a small current velocity of $U_c = 0.1$ m/s. The water depth is set the same as the physical test.

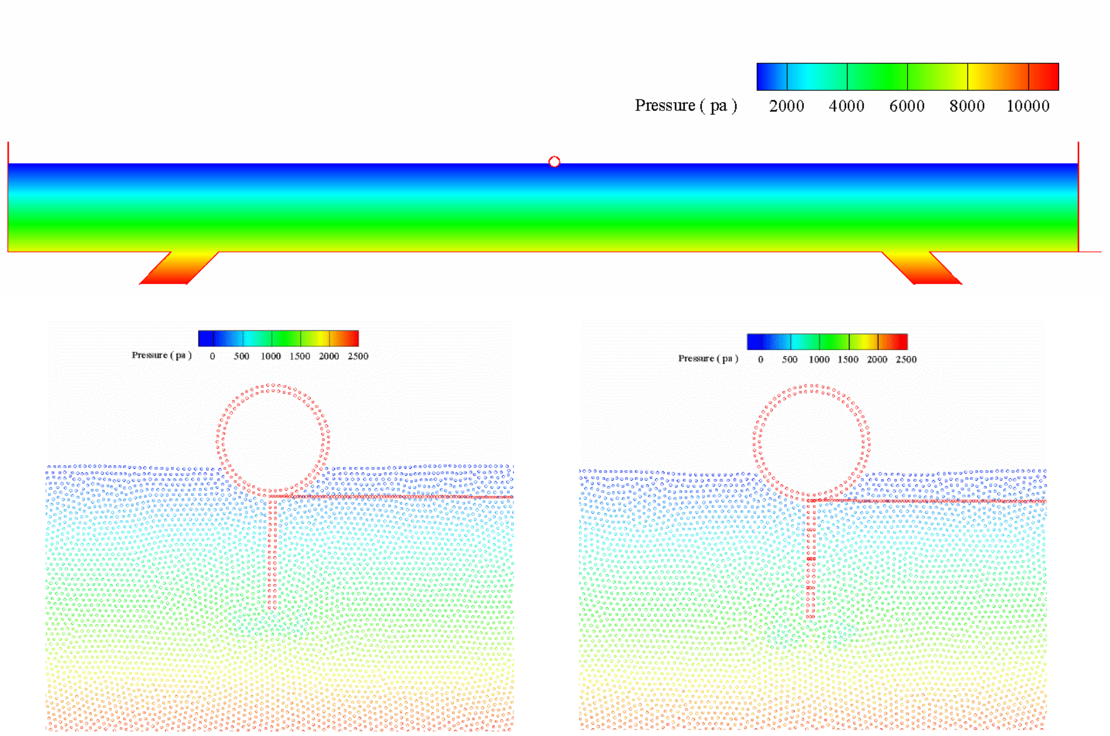

Fig. 15. Snapshots of numerical model at initial moment: general layout of water flume (top); localized layout of rigid boom (bottom left); localized layout of flexible boom (bottom right).

4.3. Calibration of the elastic coefficient of the mooring line

Since the mooring line in the SPH model is simulated by the simple spring model as shown in Eq.(19), its behavior should be greatly influenced by the spring elasticity. In this section, the effect of spring elasticity is investigated and the appropriate value of the elastic coefficient is examined by performing a series of trial calculations. A number of elastic coefficients of the mooring line are listed in Table 2 for sensitivity test.

Table 2. The elastic coefficient of the mooring line of different cases ($\times 10^3$ kg/s^2).

No.	K_1	K_2	K_3	K_4	K_5	K_6	K_7
k_t	0.01	0.1	1	5	10	50	100

The test results in Fig.16 indicate that for smaller value of the elastic coefficient, e.g. $k_t = 0.01\times10^3$ kg/s^2, stretched length of the mooring line will keep positive during the entire test, which means that the boom is continuously restrained by the mooring lines. For relatively larger value of the elastic coefficient, however, e.g. $k_t > 0.1\times10^3$ kg/s^2, the mooring lines are for quite a long period of time in a state of relaxation and are only for a very short time of time in a state of tension during the wave cycle. This implies that a sudden pulling must occur in the mooring lines, which is also observed in the physical test. For the case of very large value of elastic coefficient, e.g. $k_t = 100\times10^3$ kg/s^2, non-physical oscillations of the mooring line could happen at $t/T \approx 1.75$ once.

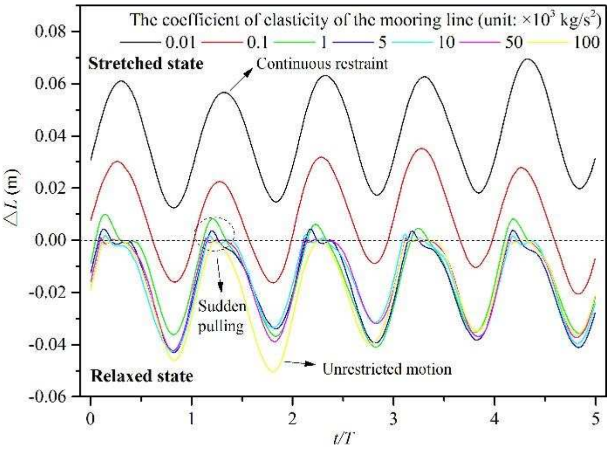

Fig. 16. Effects of elastic coefficient of the mooring line on its stretched length △L.

Due to that the mooring force exerted on the boom is mainly in the horizontal direction, it is expected that the elastic coefficient of the mooring line has a much more significant influence on the sway responses of the floating boom rather than heave and roll. To fully understand this, Fig. 17 compares the horizontal motion of the floating boom from seven different stiffness coefficients. For the very flexible spring system with $k_t \leq 0.1\times10^3$ kg/s^2, the sway responses of the boom obviously depend on the elasticity of the mooring line. When the floating boom is subject to very rigid mooring line (100×10^3 kg/s^2), non-physical extension of the mooring line could happen with unnaturally large amplitude (see in Fig. 16) and thereby leads to the non-physical oscillations of the boom in the horizontal direction. Since the sway responses of the floating boom are rather similar for the mooring line with transitional values of elastic coefficient ranging from $k_t = 1\times10^3$ kg/s^2 to 50×10^3 kg/s^2, an elastic coefficient of 5×10^3 kg/s^2 is used in the present model.

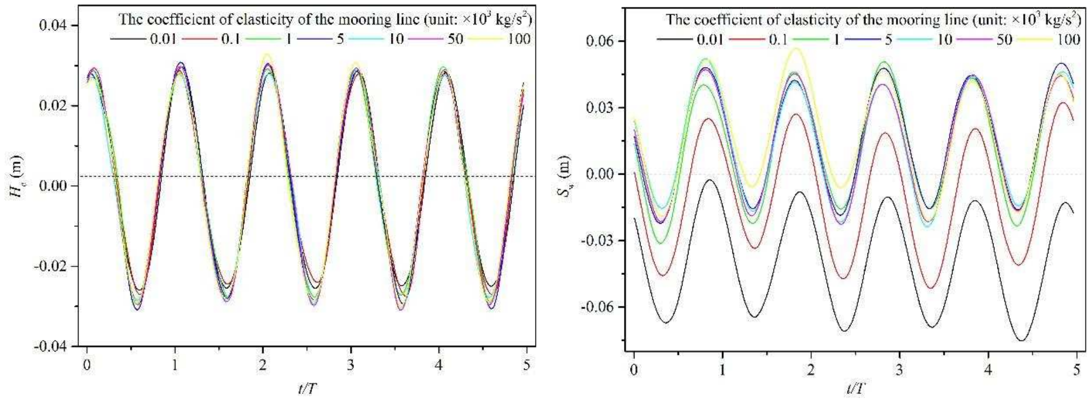

Fig. 17. Effects of elastic coefficient of the mooring line on heave H_e (left) and sway S_w (right) responses of the boom.

4.4. Calibration of translational stiffness of connector in multi-body system

The stiffness of the connector in a multi-body system is a key factor for obtaining the proper motion responses of the floating boom. Totally 8 cases of the tests were performed for the connector with different translational stiffness (Table 3). The motion parameters of the flexible boom and the horizontal and vertical force components exerted on the connector under the action of fixed wave and current conditions are recorded for selecting a reasonable connector stiffness. The variations of the total force exerted on the connector of the floater and skirt module #1 for the different stiffness (K_2~K_7 in Table. 3) are shown in Figs. 18 and 19. It is noticed that larger stiffness can effectively reduce the high-frequency noise in the tension record, while excessively large stiffness could result in overlap of the skirt modules, particle disorders and strong pressure fluctuations in the water near the floating boom (Fig. 20) and even divergence of the computation. On the other hand, improperly small stiffness could result in over-large separation between the two adjacent connectors (Fig. 20) and pressure ripples in the water around the boom structure. A proper value of the connector stiffness should be able to avoid module separation, high-frequency vibration and excessive hinge restriction. Among all the values of the translational stiffness listed in Table 3, the value 1×10^6 kg/s^2 seems to be the best choice for the joint of floater-skirt module #1 owing to its satisfactory hinge performance. For simplicity, the other spring stiffness of the connectors of the skirt modules also use the same value, by which stable pressure field (Fig. 20) are obtained.

Table 3. Connector stiffness of different cases (kg/s^2). (k_x denotes the horizontal translational stiffness, and k_z the vertical translational stiffness)

No.	K_1	K_2	K_3	K_4	K_5	K_6	K_7	K_8
k_x	1×10^3	5×10^3	1×10^4	5×10^4	1×10^5	5×10^5	1×10^6	5×10^6
k_z	1×10^3	5×10^3	1×10^4	5×10^4	1×10^5	5×10^5	1×10^6	5×10^6

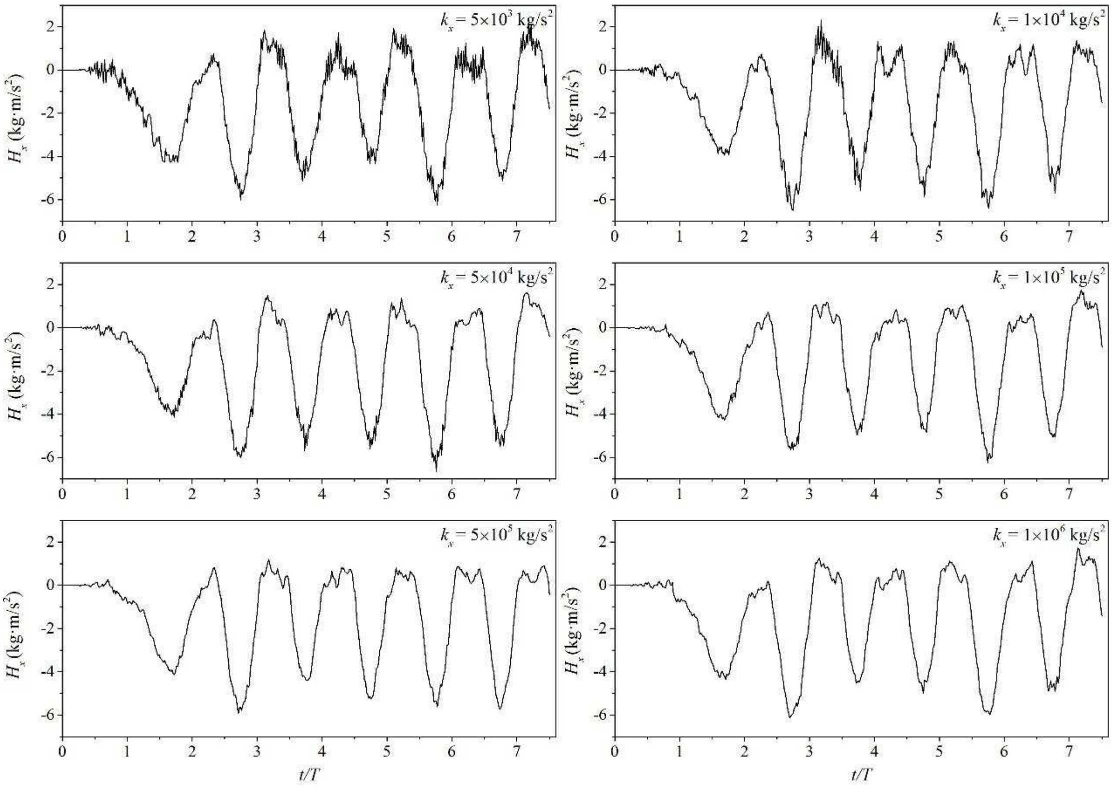

Fig. 18. Duration curves of horizontal force components H_x of connector #1.

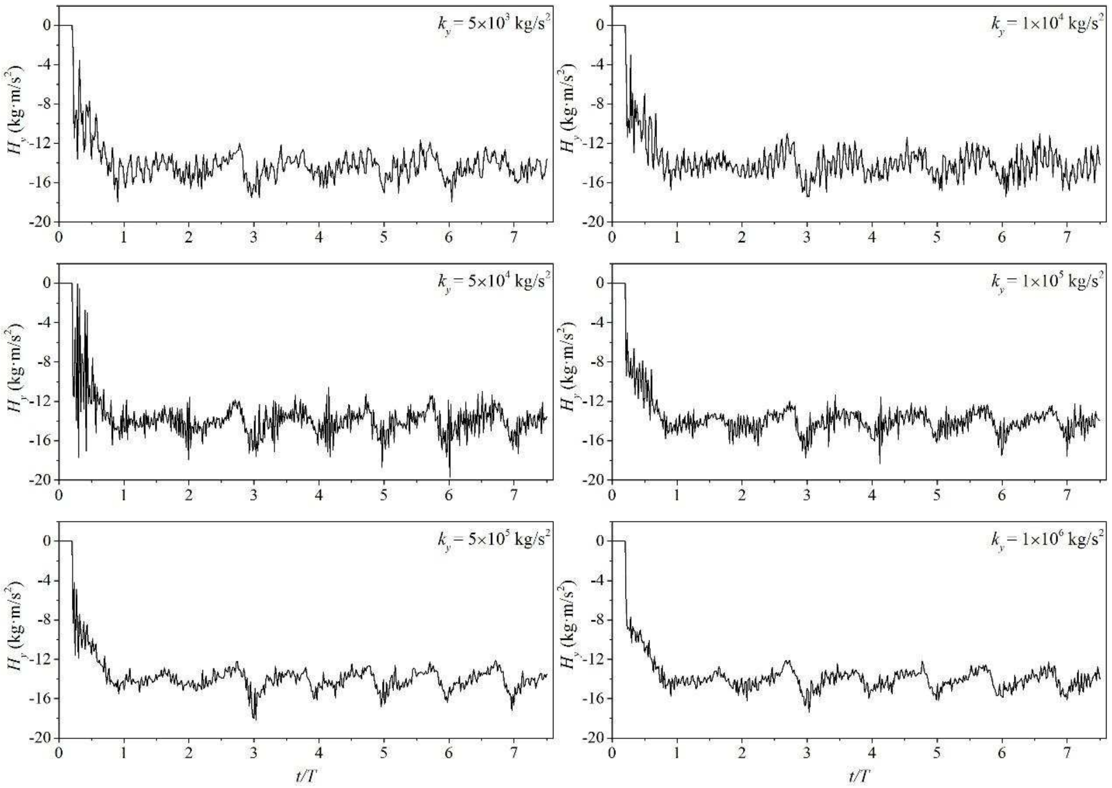

Fig. 19. Duration curves of vertical force components H_y of connector #1.

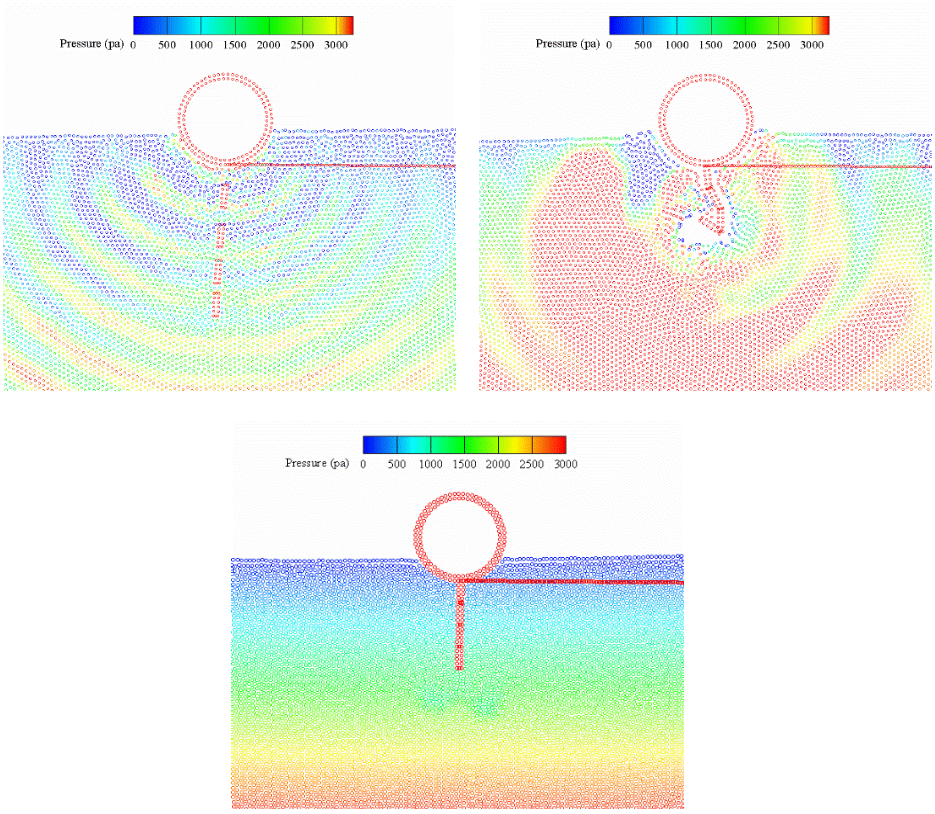

Fig. 20. Particle snapshots of flexible floating boom at t = 1.0 s by using different translational stiffness for all connectors: 1×10^3 kg/s^2 (top left); 5×10^6 kg/s^2 (top right); 1×10^6 kg/s^2 (bottom).

4.5. Wave propagation around the floating boom

To investigate wave propagation around the floating boom model, three resistance-type wave gauges were employed to observe the water surface elevations, with two on the offshore side and the third on the leeside of the floating boom (Fig. 12). Their locations (Table 4) are set to conform to the rules suggested by Goda and Suzuki (1977) for the incident-reflection wave decomposition.

Table 4. Coordinates of the wave gauges (X denotes the coordinates with respect to the location of the initial centroid of the floater, and X is positive right-wards).

No. of wave gauges	WG1	WG2	WG3
Relative position X (m)	+ 1.0	+ 0.5	-0.5

The modeled results of water surface elevation η are compared with the measured data for the rigid and flexible floating booms (Fig. 21), which shows a favorable agreement. Secondary wave in the results of WG2 (front side) and relatively smaller wave height in WG3 (rear side) indicate the effect of partial wave reflections from the floating boom. To further illustrate the effect of flexibility of the floating boom on wave reflection, the incident-reflected wave separation is performed based on the records of wave gauge WG1 and WG2. The reflection coefficient K_r, the transmission coefficient K_t and energy dissipation coefficient K_d are defined as H_r/H_i, H_t/H_i, $1-(H_r/H_i)^2-(H_t/H_i)^2$, respectively and the results are shown in Table 5. It is worthy noticing that the reflection of the flexible boom is even larger than that of the rigid one, while the wave transmission through the rigid boom is less than the flexible one. This implies more wave energy is dissipated by the rigid boom than that by the flexible one.

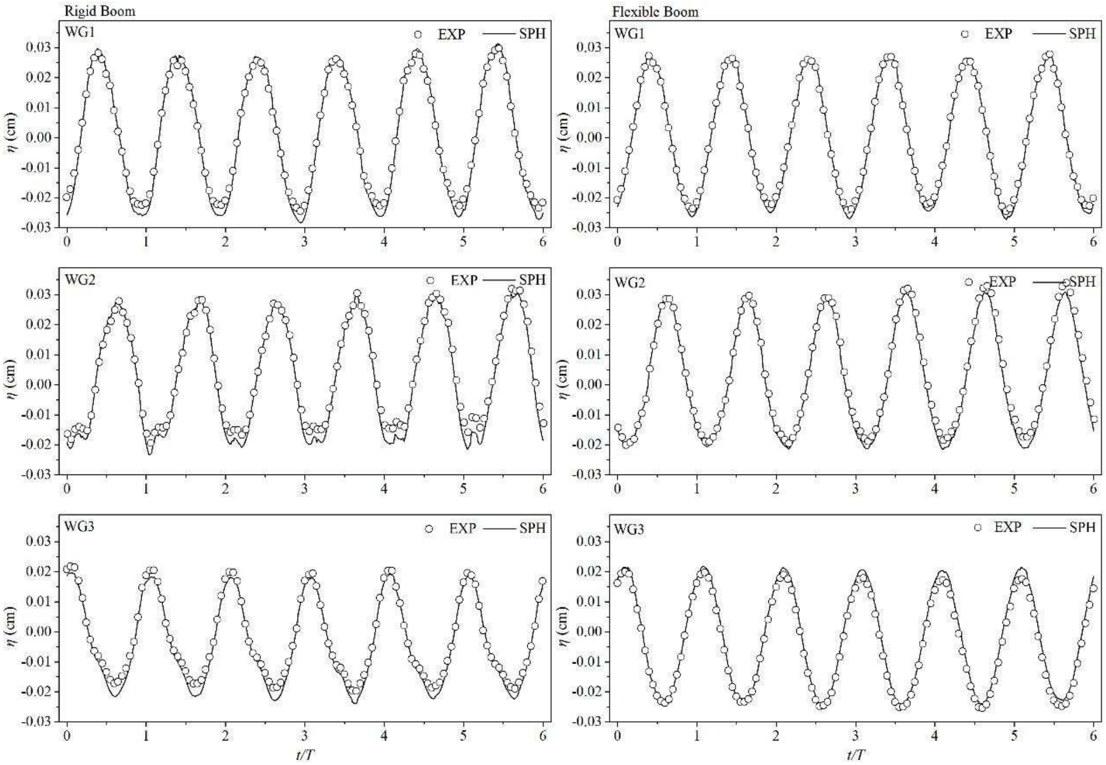

Fig. 21. Comparisons between modeled and experimental water surface elevation for the rigid boom (left) and flexible boom (right) subject to wave and current condition, H = 0.06 m, T = 1.2 s and U_c = 0.10 m/s.

Table 5. Reflection, transmission and energy dissipation coefficients of floating boom.

Model type	**Reflection coef. K_r**		**Transmission coef. K_t**		**Dissipation coef. K_d**	
	Num.	Exp.	Num.	Exp.	Num.	Exp.
Rigid	0.328	0.336	0.706	0.729	0.393	0.356
Flexible	0.347	0.360	0.792	0.785	0.252	0.254

4.6. Simulation of motion of floating boom

Figs. 22 and 23 show the consistency between the observed and modeled results of the instantaneous snapshots of the ambient water surface and boom pose by using rigid and flexible booms, respectively. It is seen from both the modeled and the observed results that when wave crest approaches [Figs. 22 (a) and (b)], the boom tends to rotate in the clockwise direction because its upper joint is restricted by the mooring line and its bottom end keeps moving shoreward due to its inertia. At this moment slight water blockage occurs on the offshore side of the boom due to the effect of current [Fig. 22 (b)]. After passing over of the wave crest the boom starts to rotate counterclockwise until it stands in an upright pose [Fig. 22 (c) and Fig. 22 (d)] on the wave trough. The counterclockwise rotation will continue due to the inertia effect until the next wave crest comes.

The consistency can also be seen from the similarity of the modeled skirt deformation of the flexible boom with the experimental image (Fig. 23). For a flexible boom, the floater and the skirt move separately in the way that they all tend to lean in the offshore direction under the wave-current coupling condition due to its flexibility [Figs. 23 (b) and (c)]. The skirt of the flexible boom moves in a similar manner with the rigid one except its bending deformation, while the floater is relatively more complicated as indicated later.

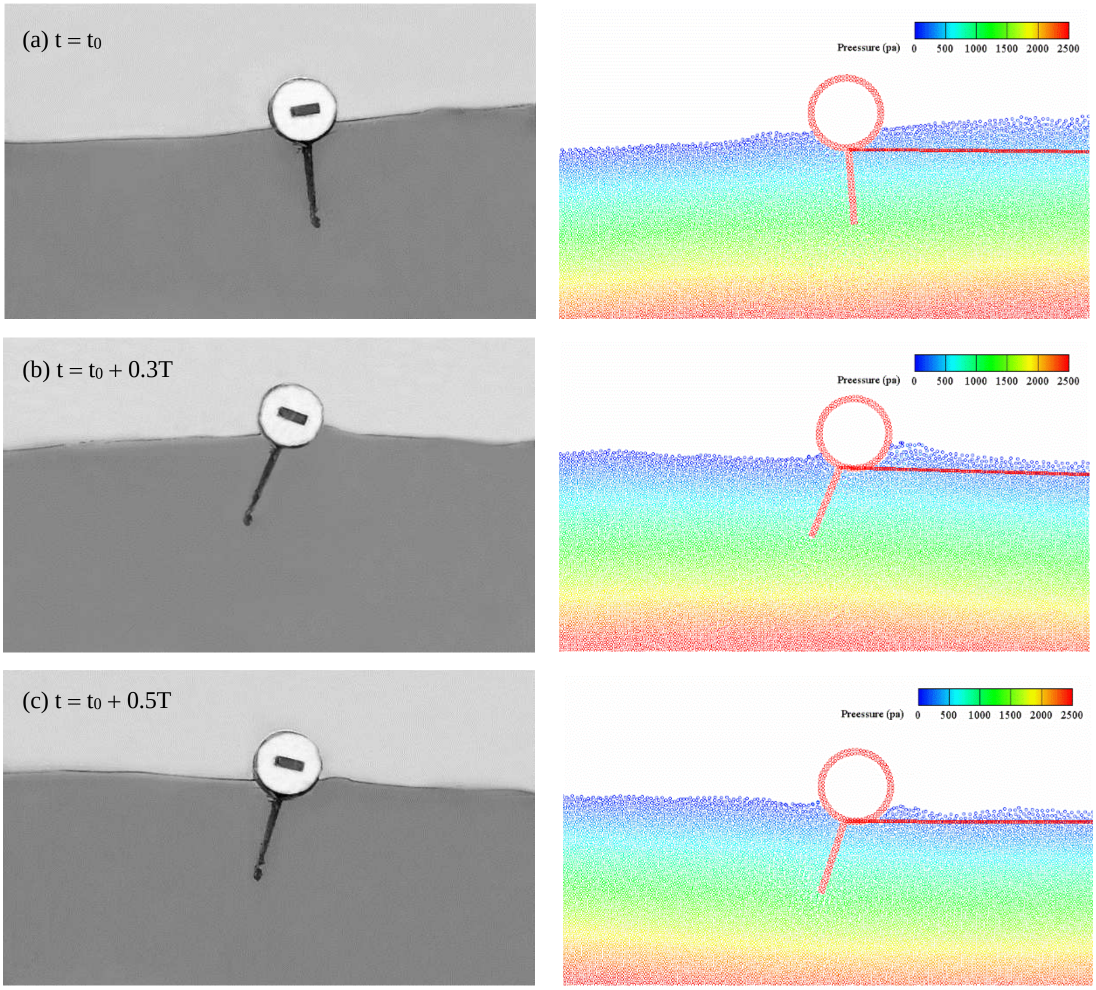

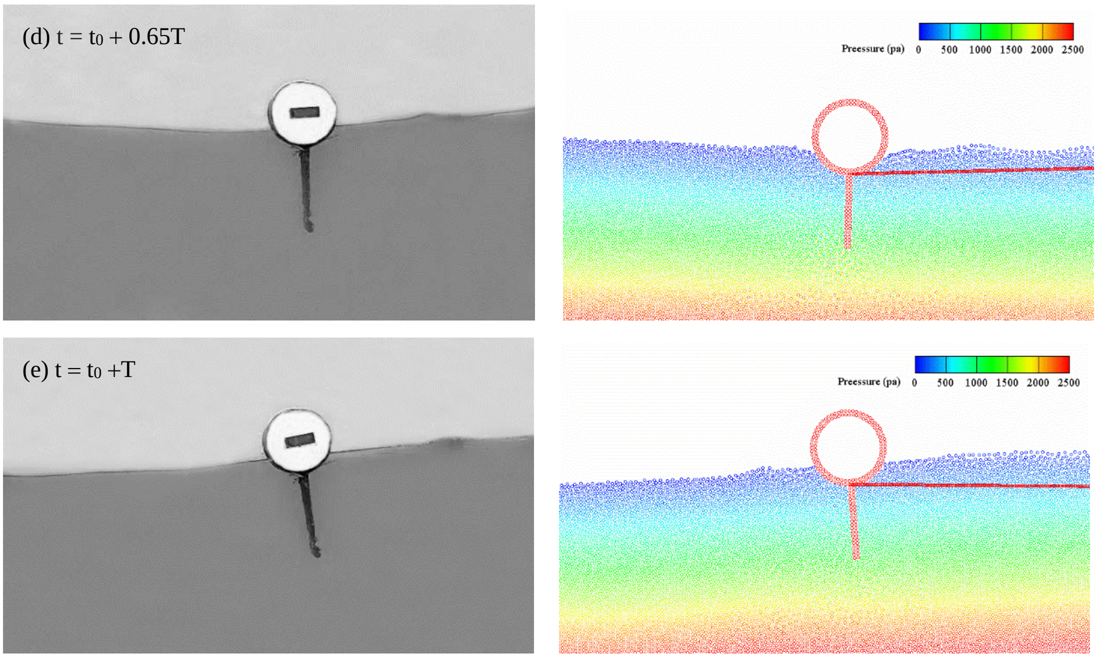

Fig. 22. Snapshots of wave profiles and poses of rigid floating boom in a wave cycle: physical experiment (left), and SPH simulation (right).

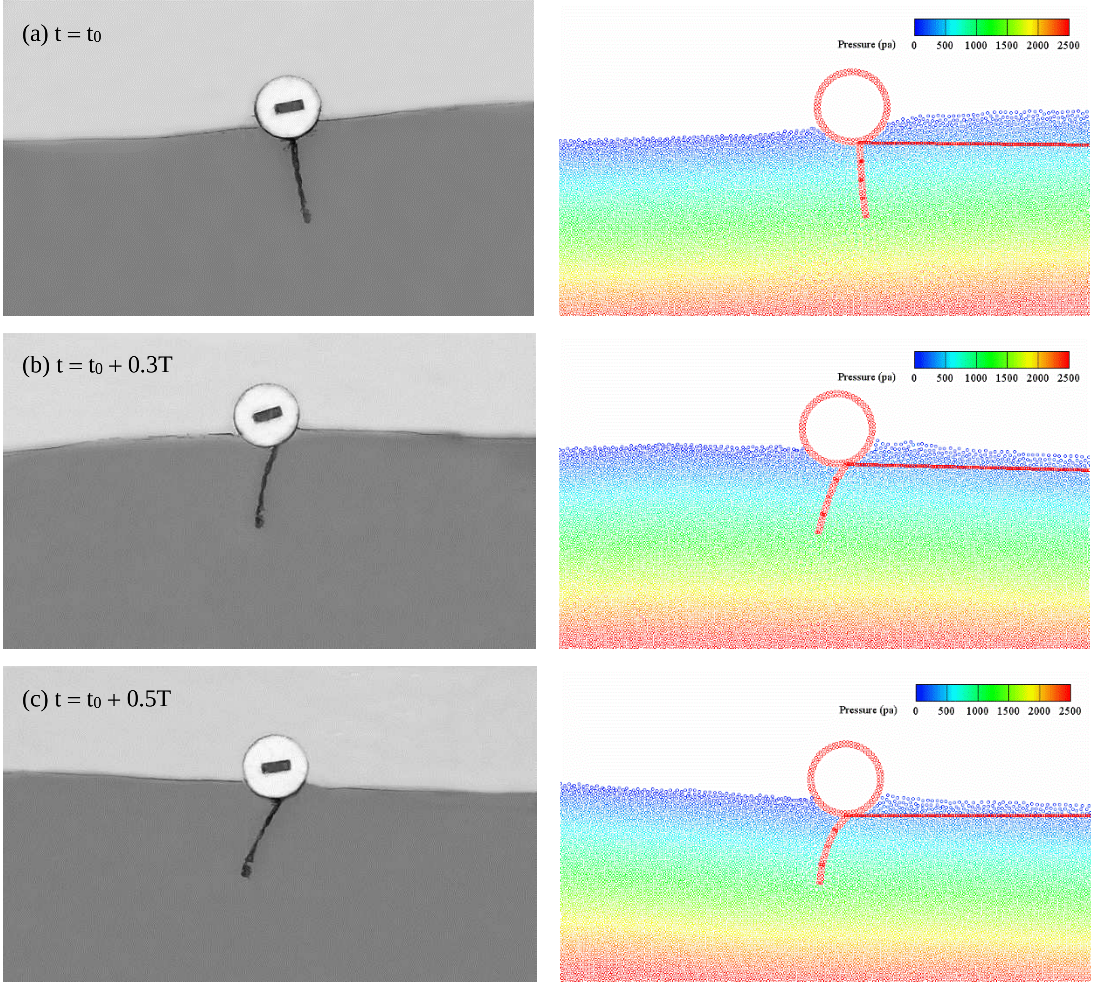

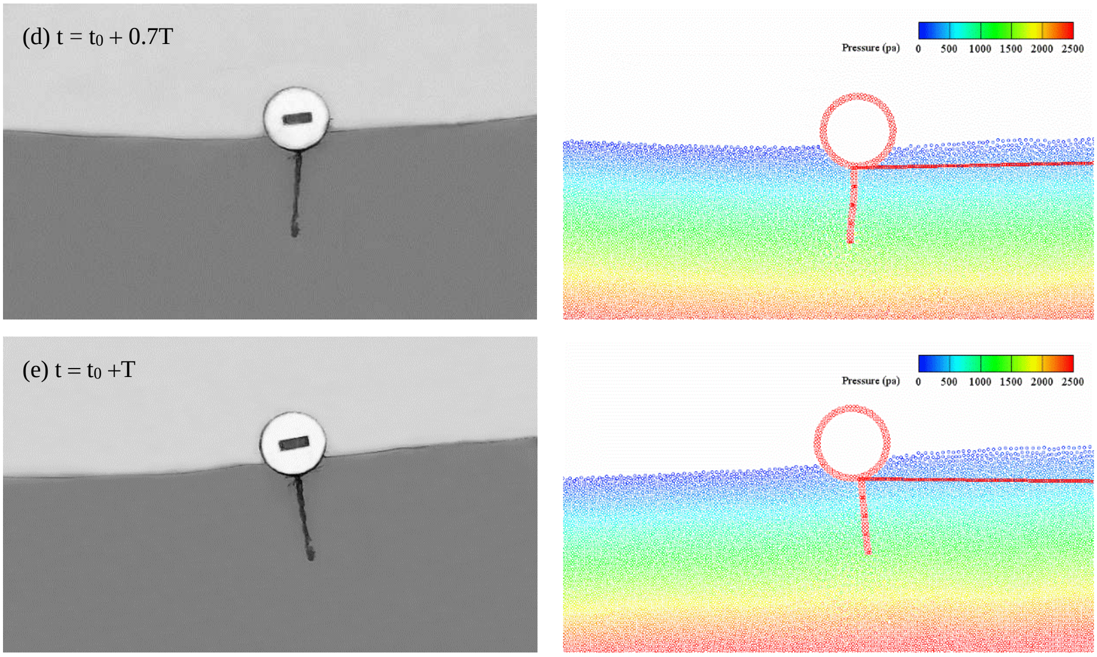

Fig. 23. Snapshots of wave profiles and poses of flexible floating boom in a wave cycle: physical experiment (left), and SPH simulation (right).

Monitoring of the rigid boom motion is performed via records of the trajectory of points P_1 and P_2 (Fig. 3). For the flexible one, the motion of the skirt is monitored by additional two points P_3 and P_4. The modeled and measured results of the heave, sway and roll motions are compared for the rigid and flexible booms in Fig. 24. Nine dimensionless characteristic time instants (i.e., $t_1 = t_0$, $t_2 = t_0 + 0.3T$, $t_3 = t_0 + 0.5T$, $t_4 = t_0 + 0.65T$, $t_4' = t_0 + 0.7T$, $t_5 = t_0 + T$, $t_6 = t_0 + 0.15T$, $t_7 = t_0 + 0.35T$, and $t_8 = t_0 + 0.85T$) are marked in the figure for the convenience of analysis. The instant t_4' occurs only in the flexible boom test. The moments t_1, t_2, t_3, t_4 (t_4'), t_5 in Fig. 24 correspond to the snapshots in Figs. 22 and 23 (a)-(e), respectively. In general, the modeled results show favorable agreement with the measured ones. There are no considerable differences in the results of heave between rigid and flexible booms. Small differences exist in the results of sway between the flexible and rigid boom, while significant differences exist in the roll responses due to the deflection of the skirt body. Slight reduction of the sway amplitudes of the flexible boom is also attributed to the deflection of the skirt and the consequent reduction of its drag area. The reduction of the sway response of the floater may be attributed to its linkage to the skirt.

Regarding the rigid boom, the duration curve of the heave responses shows a nonlinear feature of slow increasing in the duration between t_1 and t_2 and quick declining in the duration between t_2 and t_3. After the heave movement has passed its peak at instant t_2, the floating boom will continue its translation and rotation until time instant t_7 when the wave crest passes over. At this moment t_7, both the sway and roll responses achieve their extreme values. Hereafter, the boom translation and rotation are reversed until time instant t_8 when they simultaneously achieve their next extreme values. The floating boom cannot return to its initial upright position at the instant t_4 and t_6 because of the effect of current action.

The heave motions of the floater and skirt of the flexible floating boom [Fig. 24 (right)], on the other hand, are almost in phase and have nearly the same magnitude. The phases of the sway of the skirt are approximate T/4 ahead of the phase of the heave. A slight phase lag T/8 exists between the sway motion of the floater and the skirt. At instant t_4' and t_6, both the sway and roll responses of the floater keep consistent with those of the skirt. Starting from the instant t_6 both the floater and skirt continue to move towards the offshore direction and reach their extremum at instant t_7. The trough values of the sway of the skirt is larger than that of the floater, which can be attributed to the skirt flexibility, while the sway magnitudes of the floater and skirt show opposite tendency from time instant t_4' and later on, which shows declining tendency for the floater and increasing tendency for the skirt. It is interesting to notice that there are two pairs of peak and trough within one wave cycle for the roll responses of the floater, which can be attributed to the effects of sudden pulling of the mooring line at instant t_6. The roll magnitude of the first trough (at instant t_7) is larger than the second one (at instant t_1). The roll responses of the floater of the flexible boom are out of phase with those of the skirt in the period between t_6 and t_4', while keep in phase after heave responses attains its minima at instant t_4'.

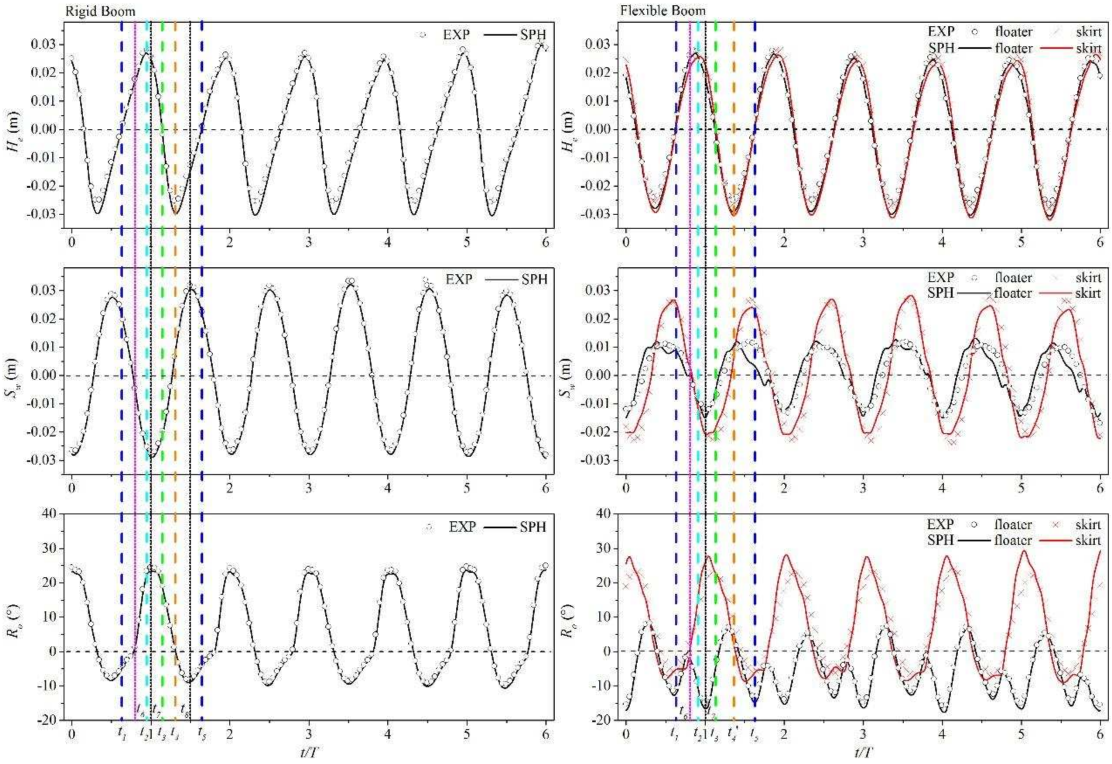

Fig. 24. Comparisons between modeled and measured results of heave H_e, sway S_w and roll R_o responses of the rigid boom (left) and flexible boom (right).

Modeled results of the tension of the mooring line exhibits periodic and impulsive features over one wave cycle (Fig. 25), which is different from the continuous action of water pressure (Fig. 26). The impulsiveness implies that the wave force dominates the current. Roughly, the horizontal components of the tension of the mooring line and the net wave force acting on the floating boom are one order greater in the magnitude than the vertical ones. The maxima of the tension in the mooring lines and wave forces exerting on the rigid floating boom are approximately two times those of the flexible one.

The duration curves of the wave force and the tension of mooring line of the rigid boom show an uneven double-peak shape (Figs. 25 and 26), which is different from the relatively flattened crest of the flexible boom due to its flexibility. The first peak of the rigid boom corresponds to the upright pose of the boom and the second peak corresponds to phase of the maximum displacement of the boom in the onshore direction. The trough behind the first peak corresponds to the phase of the extremum of heave, sway and roll motion, during which the water pressure is released gradually due to the rotation of the boom.

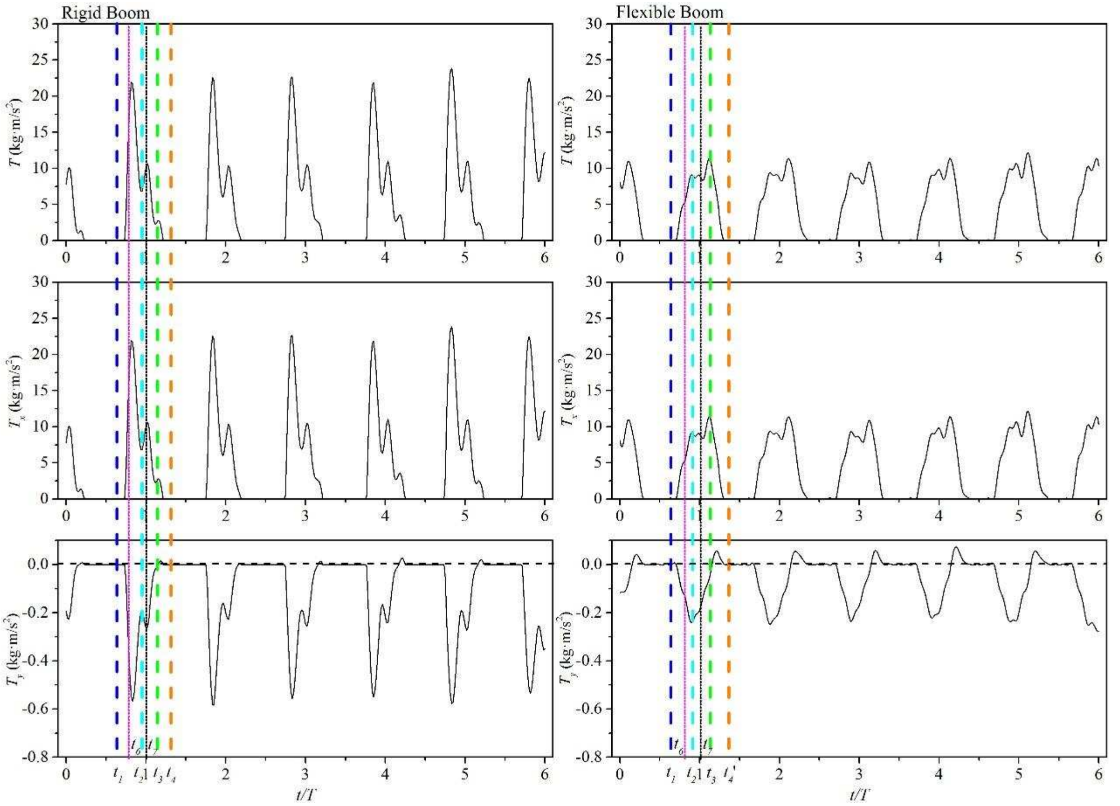

Fig. 25. Simulated results of time series of mooring forces for the rigid boom (left) and flexible boom (right). T, T_x, T_y denote total, horizontal and vertical mooring forces, respectively.

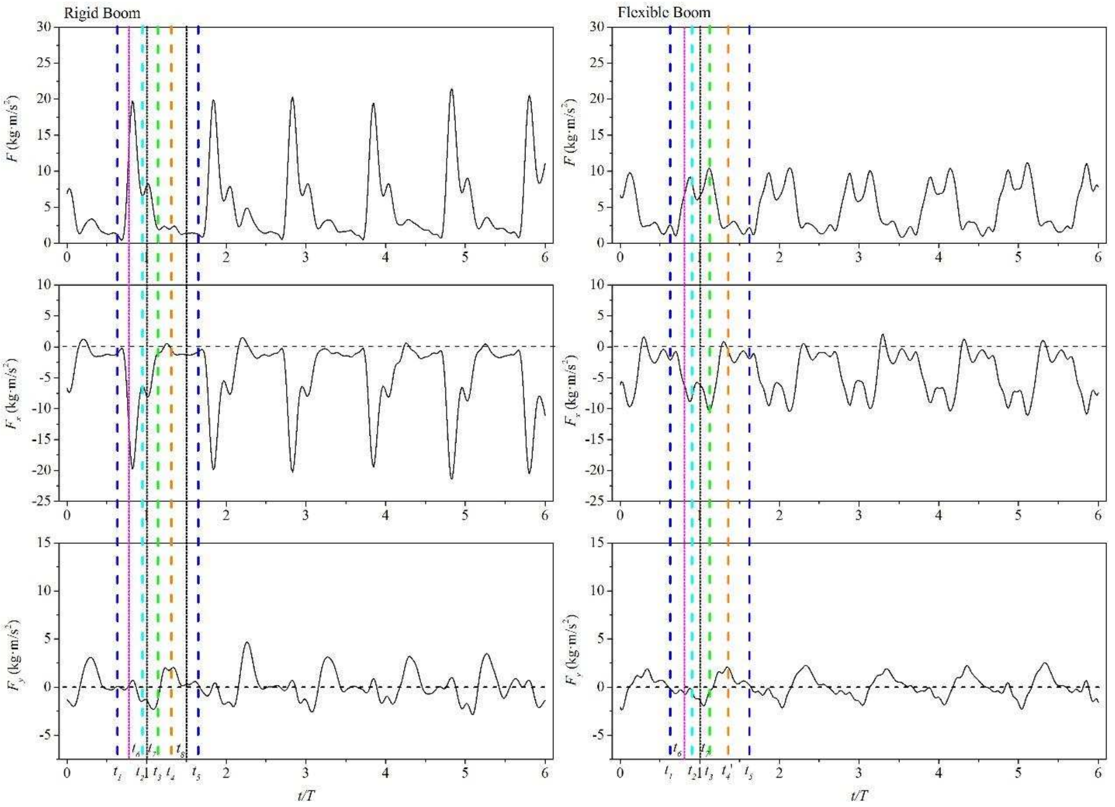

Fig. 26. Simulated results of time series of net wave forces for the rigid boom (left) and flexible boom (right). F, F_x, F_y denote total, horizontal and vertical wave forces, respectively.

5. MODEL APPLICATION II: OIL CONTAINMENT AND FAILURE PROCESS UNDER COUPLED CURRENT-WAVE CONDITION

The WCSPH model of the present study is applied to simulating an oil slick evolution process. The numerical wave flume is the same as described in Sec. 4.2 except that the spilled oil is considered in this section. The industrial gear lubricant CKC680 (with rheological characteristics shown in Fig. 7, and molecular viscosity and reference density being 1625 mm^2/s and 890 kg /m^3, respectively) was poured on the upper layer beyond the water surface with initial slick thickness 0.02 m and slick length 1 m (Fig. 12). The initial particle spacing is also taken as 0.005 m for all the particles. For the case of the rigid boom, totally 328521 particles are employed in the computation, including 5298 solid particles, 321851 water particles and 1372 oil particles. In comparison, for the case of the flexible boom, totally 328537 particles are employed, including 5314 solid particles, 321851 water particles and 1372 oil particles. The total simulation time is set as 25 s and the CPU time is nearly 3 days 20 h.

Flume tests were performed for different current velocity, wave parameter and boom flexibility. The tests were carried out according to the following steps: (i) Oil was initially poured on the upstream of the boom to form a thin oil slick; (ii) Current velocity was imposed for a specified time period at an increment of about 0.01 m/s controlled through the computer until the oil slick reached a stable state; (iii) The free surface shape of the oil slick was recorded throughout the process; (iv) Steps ii and iii were repeated until the containment failure of oil happened. Tests of the wave-coexistence situation were carried out at a constant flow condition.

5.1. Effect of approaching current velocity

Fig. 27 shows the modeled snapshots of oil slick evolution at different stages from the shortening and thickening to the containment failure. The snapshots of the experiment at the corresponding stages are also presented as a comparison. At the low approaching current velocity stage, most part of the oil slick is spread uniformly in front of the boom except a little bit heaping-up near the boom bottom [Fig. 27 (a)]. The modeled slick profiles seem a little bit thicker than the experimental ones at lower current velocity [Fig. 27 (a) and (b)]. Some important factors, such as the spatial resolution, and the lack of turbulence could possibly contribute to this discrepancy. As the approaching current velocity increases, the oil slick continues to contract and thicken until a triangle cross section is formed in front of the boom skirt [Fig. 27 (c)], which is accompanied by the occurrence of a water phase vortex under the oil slick. This observation is quite different from the assumption on the shape of the oil slick from the potential flow theories (Cross and Hoult, 1971; Chebbi, 2009) that assumes a triangular-shaped oil slick in front of the oil boom. Further increase of the current velocity leads to shrinkage of the vortex in front of the boom skirt [Fig. 27 (d)] and finally oil escaping beneath the skirt tip occurs when the vortex vanishes [Fig. 27 (e)]. The escaped droplets are either caught inside the sheltered area immediately behind the floating boom or spread toward the downstream direction carried by the ambient water flow [Fig. 27 (f)]. It might be noticed that the calculated rolling angle of the skirt is considerably smaller than that of the experimental results, especially under high flow velocity conditions (Fig. 27). The reason for this deviation can be given as follows. On the one hand, the oil slick exerts smaller pressure on the front surface of the boom structure than the water due to its relatively lower density. Besides, the images shown in Fig. 27 may mislead the reader because in the physical experiment, the thickness of oil slick in the inner part of water flume is considerably thin than that near the flume side because of the viscous effect between the side wall and the oil, especially at high current velocity. This implies that in the real experiment the water actually contributes more to the pressure on the boom front face than what is shown in Fig. 27. Such uneven distribution of the oil slick in the transverse direction is not reflected in the SPH simulation.

(a) $U_c = 0.06$ m/s

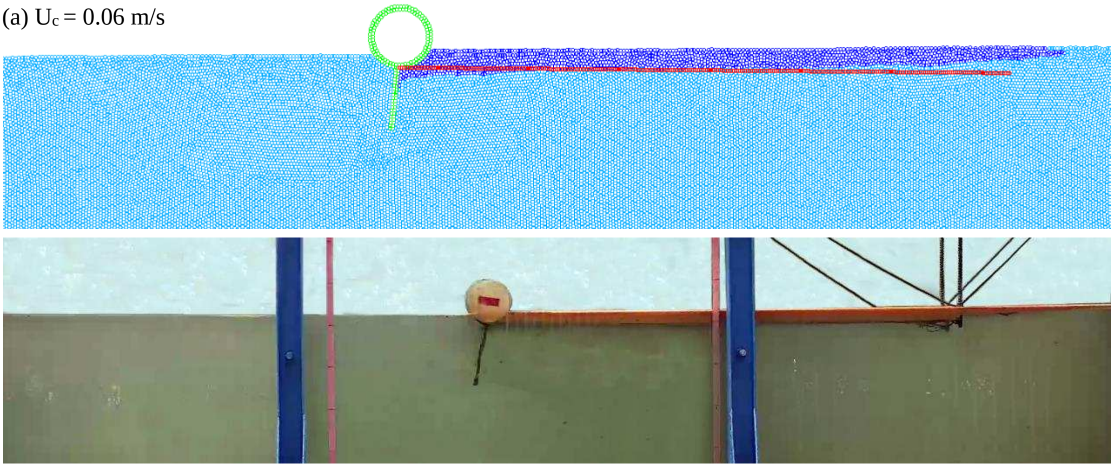

(b) $U_c = 0.15$ m/s

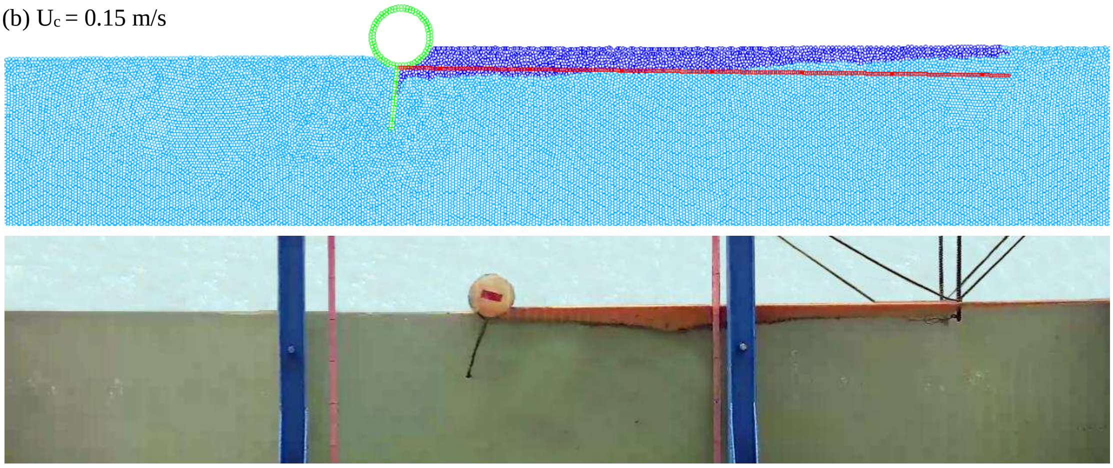

(c) $U_c = 0.27$ m/s

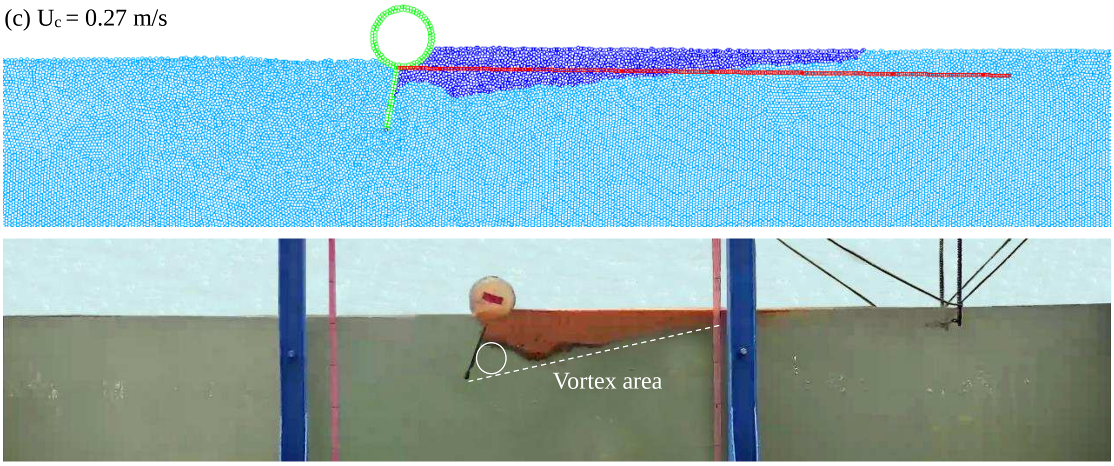

(d) $U_c = 0.40$ m/s

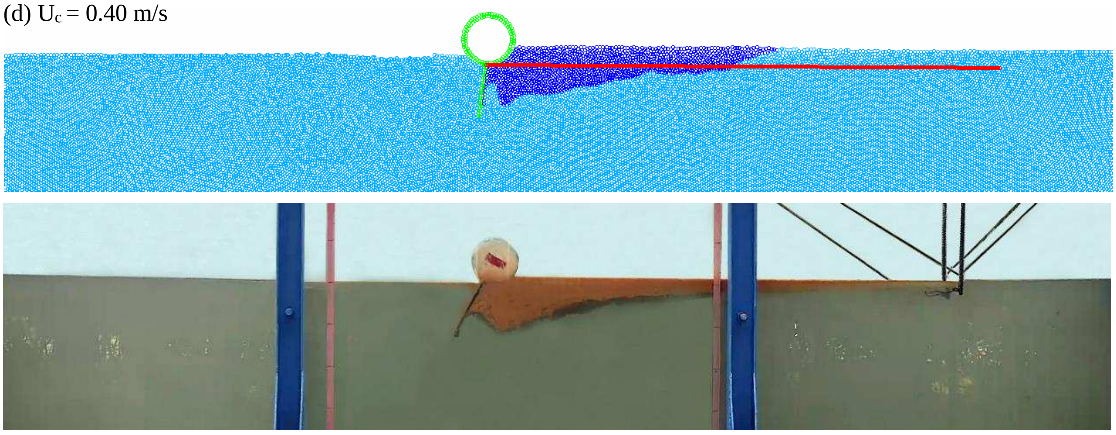

(e) $U_c = 0.48$ m/s

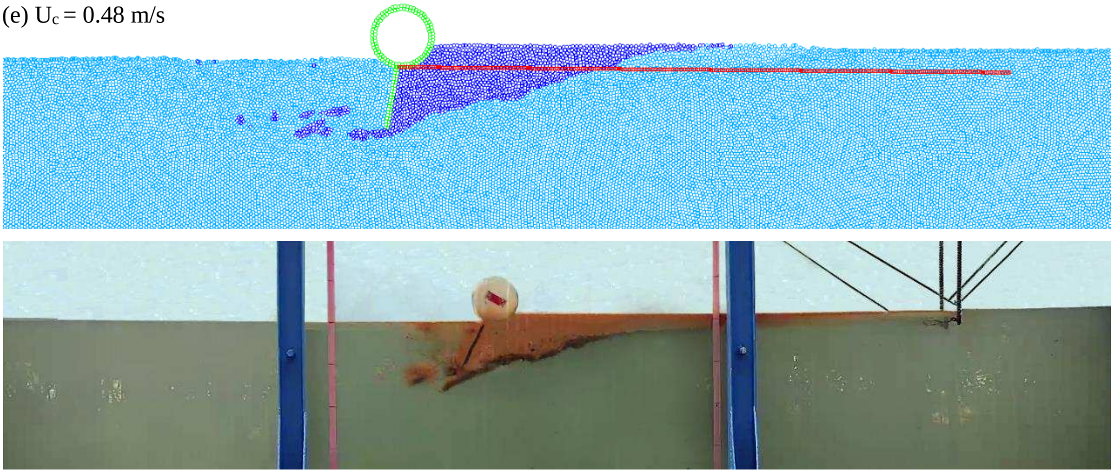

(f) $U_c = 0.66$ m/s

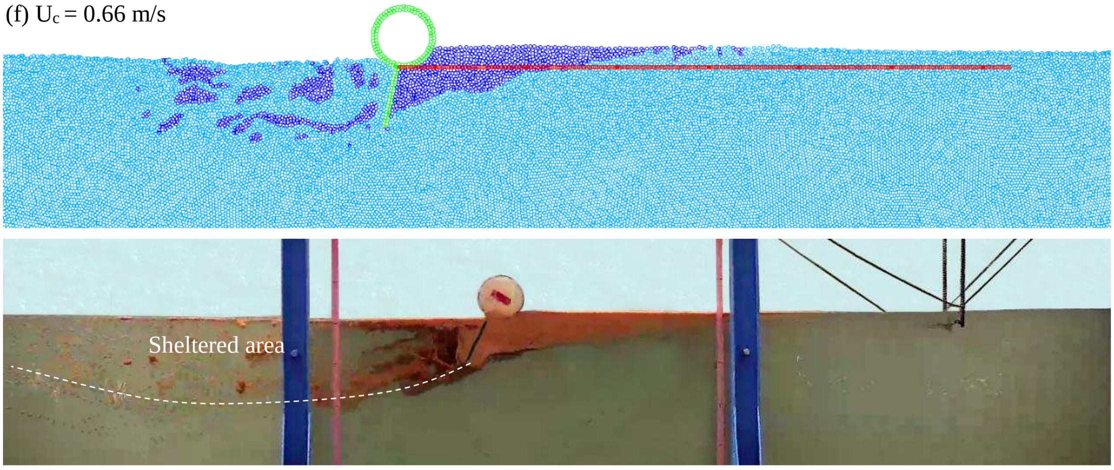

Fig. 27. The evolution process of oil slick subject to the current alone with different velocities.

The calculated velocity and vorticity distribution fields under different condition of approaching current velocities are presented in Fig. 28, where the vorticity (clockwise positive) of particle i is calculated by following Morris and Monaghan (1997), which is expressed as

$$(\nabla \times \mathbf{v})_i = \sum_j \frac{m_j}{\rho_i} \mathbf{v}_{ij} \times \nabla_i W_{ij} \qquad (23)$$

Strong vorticity is initially generated only at the tip of boom skirt [Fig. 28 (a)] and then extended in the downstream directions as the current velocity increased, which could reach to a maximum horizontal range of 7~8 times the boom draft [Fig. 28 (d)]. Vorticity are also generated along the oil-water interface when the current velocity is high [Fig. 28 (d)].

(a) $U_c = 0.18$ m/s

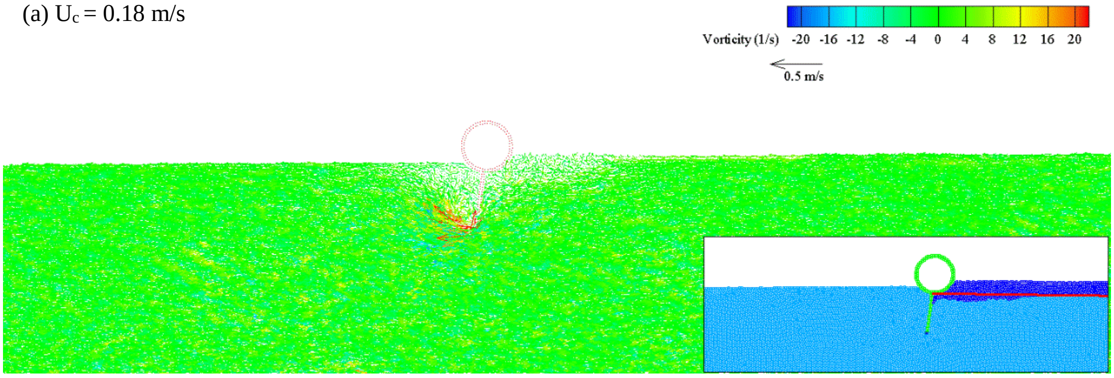

(b) $U_c = 0.30$ m/s

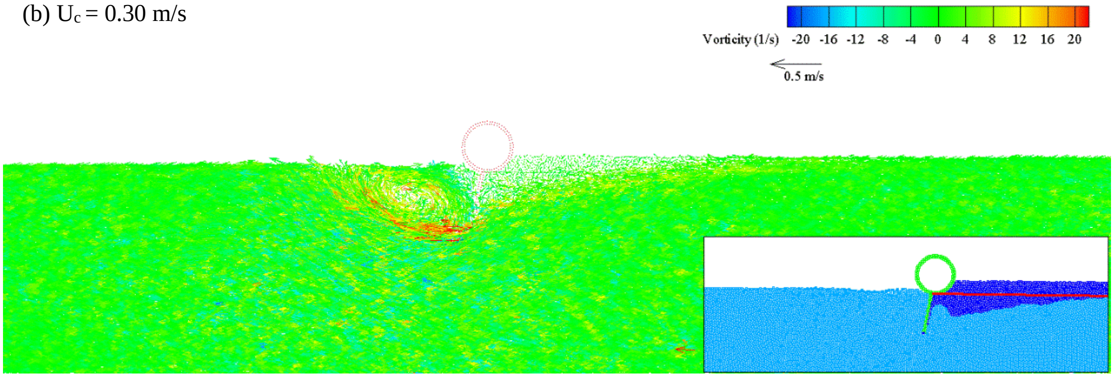

(c) $U_c = 0.54$ m/s

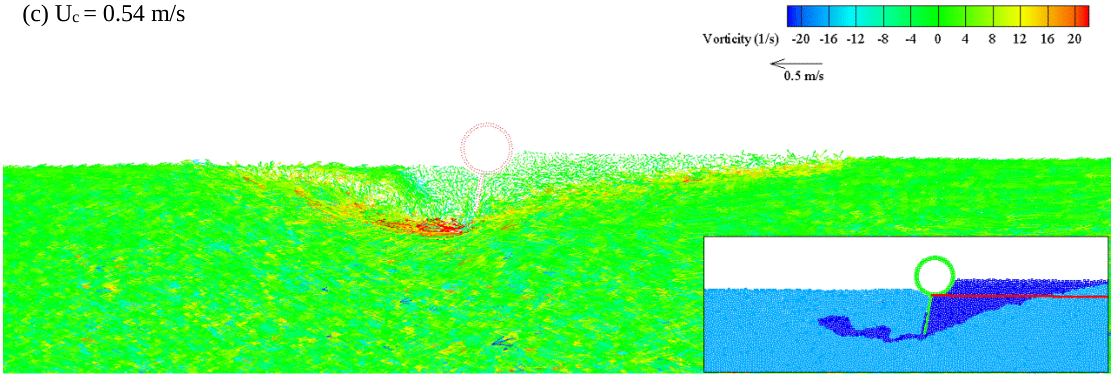

(d) U_c = 0.72 m/s

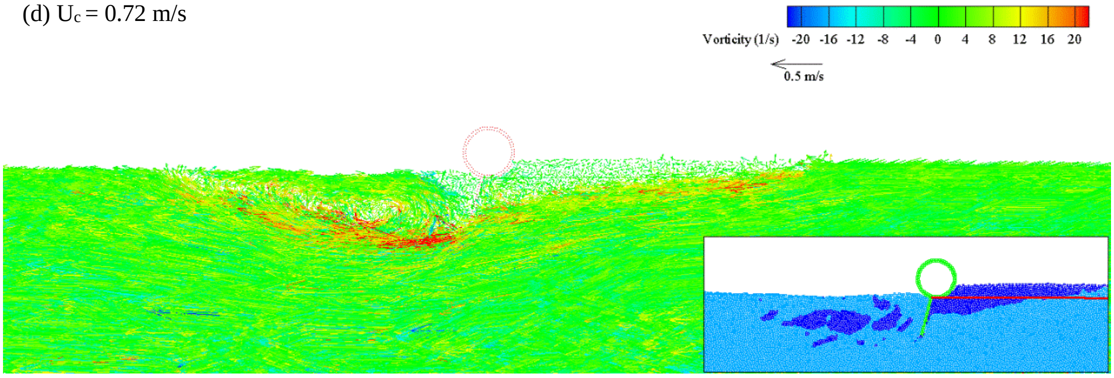

Fig. 28. Snapshots of velocity and vorticity distributions near the floating boom for the current alone.

5.2. Effect of waves

If the waves are incorporated in the test, the oil slick will become more evenly spread over the surface of the water wave, whereas the thickness of the oil slick is changeable within a wave cycle (Fig. 29). The oil slick achieves its minimum thickness when the boom is at the wave trough and achieves its maximum thickness at the wave crest.

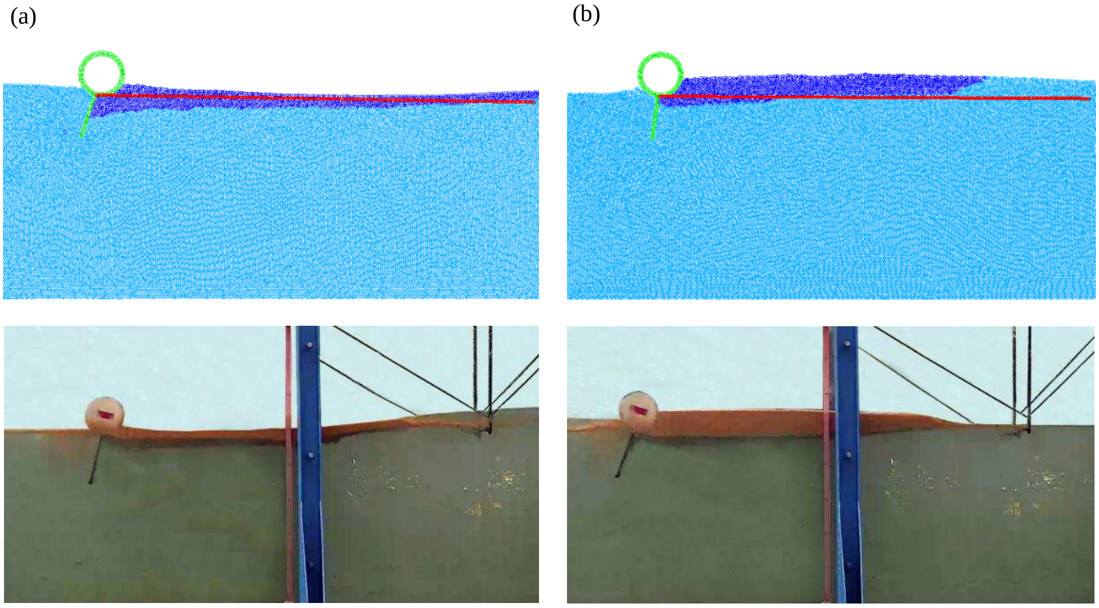

Fig. 29. Snapshots of modeled and measured results of oil slick subject to the combined wave and current (H = 0.06 m, T = 1.2 s, U = 0.2 m/s): (a) denotes boom is at wave trough; (b) denotes boom at wave crest.

Relatively larger vorticity values are concentrated on three regions, i.e. near the oil-water interface, near the tip of boom skirt, where the flow separation and vortex happen, and the sheltered area behind the boom. The wake vortex region is extended to a distance of 1~2 times the boom draft when the boom is at the wave crest and 2~3 times the boom draft when at the wave trough. Such periodical variation of the trailing vortex size under wave condition is different from the case of steady current that maintains a relatively stable region of vortex. In addition, the size of the wake vortex region under the action of combined waves and currents is much smaller than that under the current alone. This implies that the storage capacity of the sheltered area will be significantly reduced by the occurrence of waves.

(a) $t = t_0$

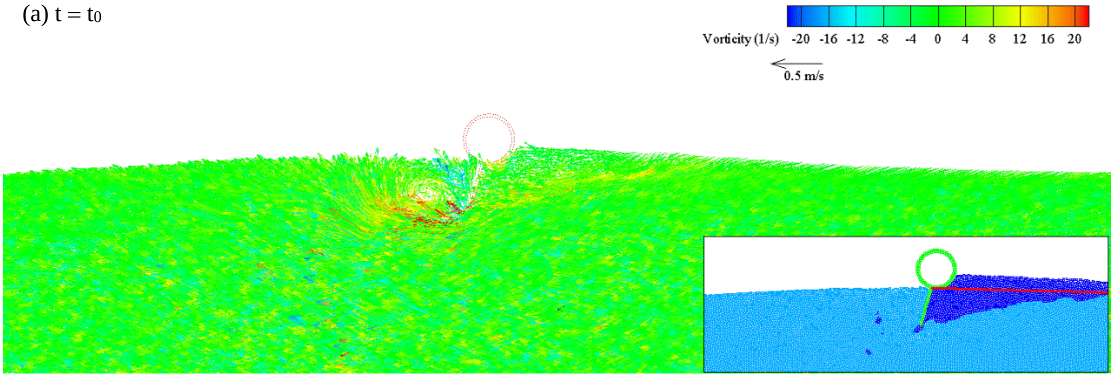

(b) $t = t_0+T/2$

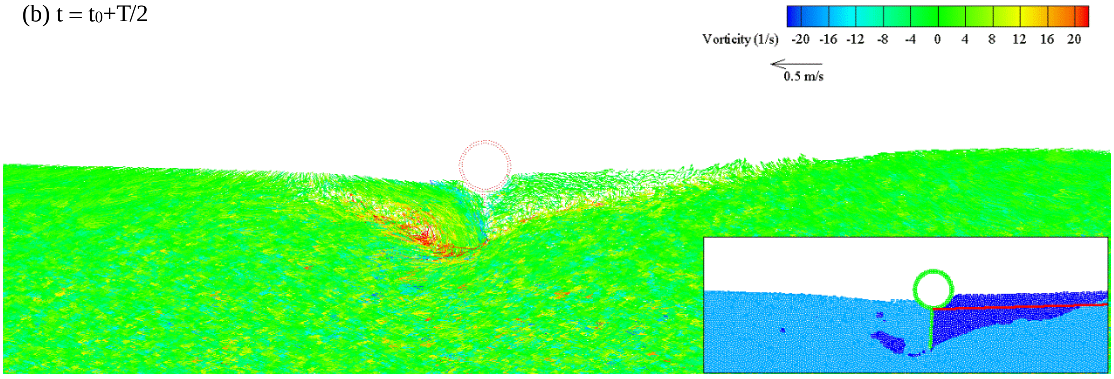

Fig. 30. Snapshots of the velocity and vorticity distributions near floating boom subject to the waves and fixed currents velocity of 0.40 m/s.

5.3. Effect of boom flexibility

Snapshots of the containment failure for the rigid and flexible floating boom are shown in

Fig. 31. It is observed that oil escaping happens for both the rigid and flexible boom for this example during the time period from t_1 to t_3 [Fig. 31 (a) - (c)]. The reason for the containment failure is mainly due to insufficiency of the boom draft. After t_4, no oil escaping from the tips of the floating boom is observed when using rigid model, whereas this happens for the flexible boom. Furthermore, the oil escaping using the flexible boom was about 5% more than that using the rigid one during the first one wave cycle after the containment failure just happens, which is indicated by that the spilled oil droplets just initially escape underneath the boom.

(a) $t_1 = t_0$

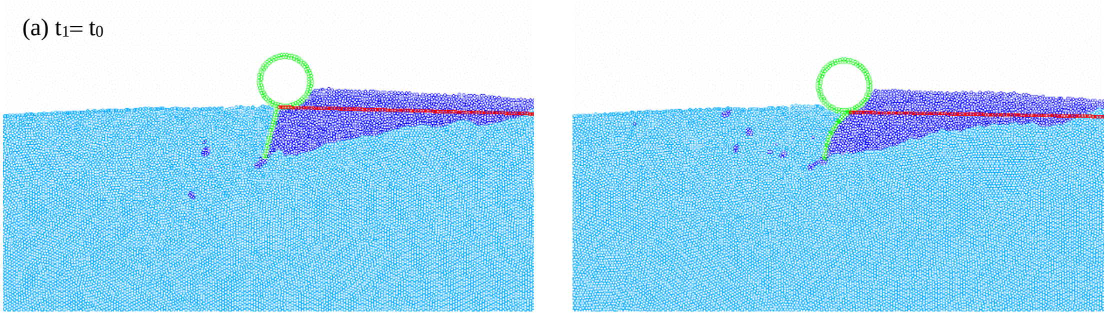

(b) $t_2 = t_0 + T/4$

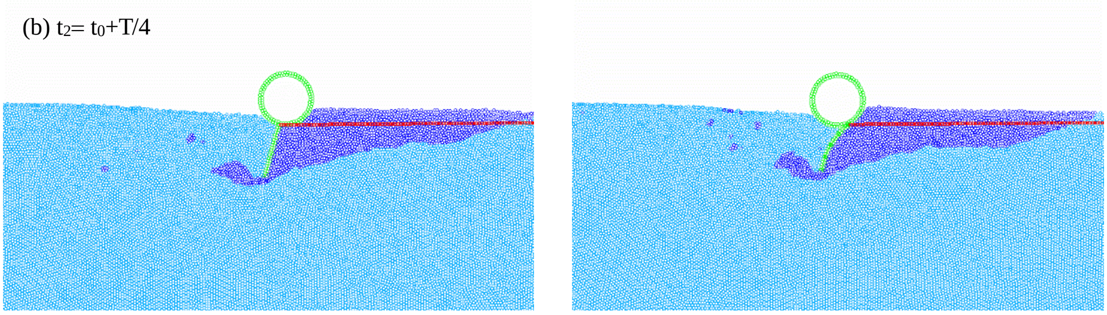

(c) $t_3 = t_0 + T/2$

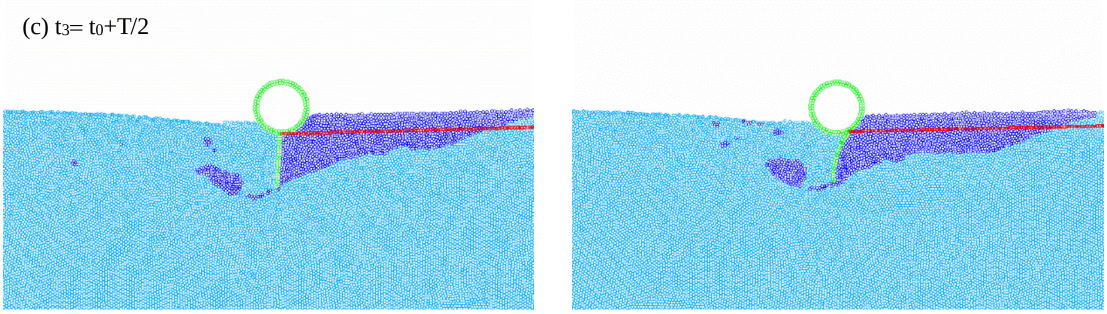

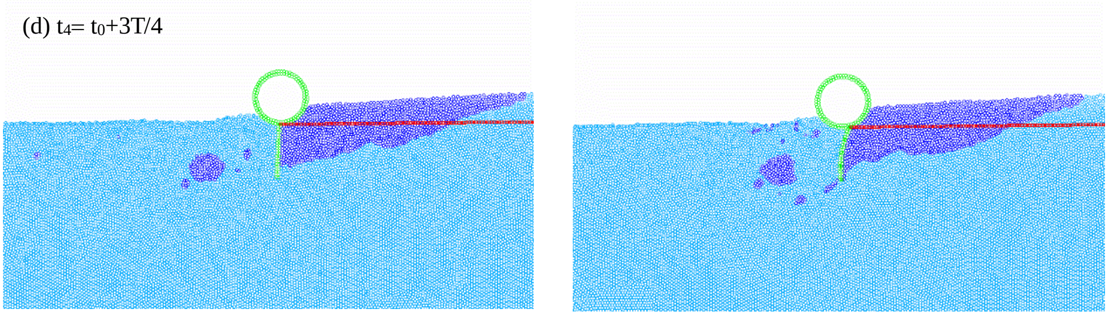

(d) $t_4 = t_0 + 3T/4$

Fig. 31. Snapshots of containment failure of rigid boom (left) and flexible boom (right) subject to the waves and fixed current velocity of 0.40 m/s.

6. Conclusions

A practical multi-phase WCSPH model is developed to simulate the spilled oil containment by a flexible floating boom under the action of coupled waves and currents. The modeled results of the vertical profile of both the steady current and combined wave-current by using the WCSPH model are well verified by the experimental data. The improved boundary treatment method for the proposed WCSPH model based on the DBPs filter is proved to be effective in reducing the numerical oscillations around the intersections of the multi-fluid interface and the solid boundary. Motions of the flexible floating boom are successively simulated by the incorporated Rigid Module and Flexible Connector (RMFC) multi-body system.

The validated numerical model is applied to investigating the movement of floating boom and oil containment process subject to the waves and currents. It is found that no significant differences exist among the heave responses of the boom with different flexibility. The roll responses of the skirt are significantly enhanced by its flexibility. The sway and roll responses are significantly influenced by the effects of sudden pulling of the mooring line.

For the last model application to the oil containment, the thickness of the oil slick is approximately in phase with the free surface elevation and tends to evenly spread due to the effect of the waves. Two vortices in the water phase exist in the front and rear of the boom skirt, and the vortex size is greatly reduced in the wave condition. The front vortex shrinks as the approaching ambient current velocity increases. Oil starts to escape via the tip of the skirt when the front vortex vanishes. The escaped oil can be trapped into the sheltered area behind the boom. The modeled results indicate that the flexible boom has relatively poor performance in containing the oil slick as compared with the rigid one. Although the motion of the flexible floating boom is successfully modeled by the present WCSPH model, simulation of the viscous effect needs further investigation in the future work.

Acknowledgements

This research is supported by the Foundation of the National Natural Science Foundation of China [Grant No.51379143], the Foundation for Innovative Research Groups of the National Natural Science Foundation of China [Grant No. 51321065] and Program of International S&T Cooperation [Grant No. S2015ZR1030].

References

Amini, A., Mahzari, M., Bollaert, E. and Schleiss, A., 2005. Fluid-structure interaction analysis applied to oil containment booms. In: International oil spill conference, pp. 585-588.

Amini, A. and Schleiss, A.J., 2009. Numerical modeling of oil-water multiphase flow contained by an oil spill barrier. Engineering Applications of Computational Fluid Mechanics, 3(2): 207-219.

American Society for Testing and Materials (ASTM), 2013. Standard F1523-94: Standard Guide for Selection of Booms in Accordance with Water Body Classifications, West Conshohocken.

An, C.F., Brown, H.M., Goodman, R.H. and Clavelle, E., 1996. Animation of boom failure processes.

Spill Science & Technology Bulletin, 3(4): 221-224.

Brown, H., Goodman, R., An, C. F. and Bittner, J., 1996. Boom failure mechanisms: comparison of channel experiments with computer modelling results. Spill Science & Technology Bulletin, 3(4): 217-220.

Chebbi, R., 2009. Profile of oil spill confined with floating boom. Chemical Engineering Science, 64(3): 467-473.

Chen, Z., Zong, Z., Liu, M. B., Zou, L., Li, H. T. and Shu, C., 2015. An SPH model for multiphase flows with complex interfaces and large density differences. Journal of Computational Physics, 283: 169-188.

Colagrossi, A. and Landrini, M., 2003. Numerical simulation of interfacial flows by smoothed particle hydrodynamics. Journal of Computational Physics, 191(2): 448-475.

Crespo, A., Gómez Gesteira, M. and Dalrymple, R.A., 2007. Boundary conditions generated by dynamic particles in SPH methods. CMC-TECH SCIENCE PRESS, 5(3): 173.

Cross, R.H. and Hoult, D.P., 1971. Collection of oil slicks. Journal of the Waterways, Harbors and Coastal Engineering Division, 97(2): 313-322.

Dalrymple, R.A. and Knio, O., 2001. SPH modelling of water waves. Coastal Dynamics' 01, pp. 779-787.

Dalrymple, R.A. and Rogers, B., 2006. Numerical modeling of water waves with the SPH method. Coastal engineering, 53(2): 141-147.

Delvigne, G.A., 1989. Barrier failure by critical accumulation of viscous oil. In: International Oil Spill Conference, pp. 143-148.

Fang, F. and Johnston, A.J., 2001. Oil containment by boom in waves and wind. I: Numerical model.

Journal of waterway, port, coastal, and ocean engineering, 127(4): 222-227.

Goda, Y. and Suzuki, Y., 1977. Estimation of incident and reflected waves in random wave experiments, Coastal engineering 1976, pp. 828-845.

Gong, K., Shao, S., Liu, H., Wang, B. and Tan, S. K., 2016. Two-phase SPH simulation of fluid–structure interactions. Journal of Fluids and Structures, 65: 155-179.

Goodman, R., Brown, H., An, C. F. and Rowe, R.D., 1996. Dynamic modelling of oil boom failure using computational fluid dynamics. Spill Science & Technology Bulletin, 3(4): 213-216.

Gotoh, H., Shibahara, T. and Sakai, T., 2001. Sub-particle-scale turbulence model for the MPS method-Lagrangian flow model for hydraulic engineering. Advanced Methods for Computational Fluid Dynamics, 9: 339-347.

Grenier, N., Antuono, M., Colagrossi, A., Touzé, D.L. and Alessandrini, B., 2009. An hamiltonian interface SPH formulation for multi-fluid and free surface flows. Journal of Computational Physics, 228(22): 8380-8393.

Hirakuchi, H., Kajima, R., Kawaguchi, T., 1990. Application of a piston-type absorbing wavemaker to irregular wave experiments. Coastal Engineering Japan, 33(1): 11-24.

Hu, X.Y. and Adams, N.A., 2006. A multi-phase SPH method for macroscopic and mesoscopic flows. Journal of Computational Physics, 213(2): 844-861.

Hu, X. and Adams, N.A., 2007. An incompressible multi-phase SPH method. Journal of Computational Physics, 227(1): 264-278.

Johnston, A.J., Fitzmaurice, M.R. and Watt, R.G., 1993. Oil spill containment: Viscous oils. In: International Oil Spill Conference, pp. 89-94.

Klopman, G., 1994. Vertical structure of the flow due to waves and currents, part 2: Laser-doppler flow measurements for waves following or opposing a current, Deltares (WL).

Liu, M.B. and Li, S.M., 2016. On the modeling of viscous incompressible flows with smoothed particle hydro-dynamics. Journal of Hydrodynamics, Ser. B, 28(5): 731-745.

Lo, E.Y. and Shao, S., 2002. Simulation of near-shore solitary wave mechanics by an incompressible SPH method. Applied Ocean Research, 24(5): 275-286.

Monaghan, J., 1989. On the problem of penetration in particle methods. Journal of Computational Physics, 82(1): 1-15.

Monaghan, J. and Kos, A., 1999. Solitary waves on a cretan beach. Journal of waterway, port, coastal, and ocean engineering, 125(3): 145-155.

Monaghan, J.J. and Rafiee, A., 2013. A simple SPH algorithm for multi-fluid flow with high density ratios. International Journal for Numerical Methods in Fluids, 71(5): 537-561.

Morris, J. and Monaghan, J., 1997. A switch to reduce SPH viscosity. Journal of Computational Physics, 136(1): 41-50.

Ren, B., He, M., Dong, P. and Wen, H., 2015. Nonlinear simulations of wave-induced motions of a freely floating body using WCSPH method. Applied Ocean Research, 50: 1-12.

Riggs, H. and Ertekin, R., 1993. Approximate methods for dynamic response of multi-module floating structures. Marine Structures, 6(2-3): 117-141.

Riggs, H., Ertekin, R. and Mills, T., 1998. Impact of connector stiffness on the response of a multi-module mobile offshore base. In: The Eighth International Offshore and Polar Engineering Conference.

Rogallo, R.S. and Moin, P., 1984. Numerical simulation of turbulent flows. Annual review of fluid mechanics, 16(1): 99-137.

Violeau, D., Buvat, C., Abed-Meraïm, K. and De Nanteuil, E., 2007. Numerical modelling of boom and oil spill with SPH. Coastal Engineering, 54(12): 895-913.

Wendland, H., 1995. Piecewise polynomial, positive definite and compactly supported radial functions of minimal degree. Advances in Computational Mathematics, 4(1): 389-396.

Wicks III, M., 1969. Fluid dynamics of floating oil containment by mechanical barriers in the presence of water currents. In: International Oil Spill Conference, pp. 55-106.

Wilkinson, D.L., 1972. The dynamics of contained oil slicks. Journal of the Hydraulics Division, ASCE, 98:1013–1030.

Yang, X. and Liu, M., 2013. Numerical modeling of oil spill containment by boom using SPH. Science China Physics, Mechanics and Astronomy, 56(2): 315-321.

Yang, X., Liu, M. and Peng, S., 2014. Smoothed particle hydrodynamics and element bending group modeling of flexible fibers interacting with viscous fluids. Physical Review E, 90(6): 063011.